AMERICAN
METEOROLOGICAL
SOCIETY

Monthly Weather Review

The DOI for this manuscript is doi: 10.1175/2010MWR3318.1

A NUMERICAL STUDY OF THE EVOLVING CONVECTIVE BOUNDARY LAYER AND OROGRAPHIC CIRCULATION AROUND THE SANTA CATALINA MOUNTAINS IN ARIZONA. PART II: INTERACTION WITH DEEP CONVECTION

J. Cory Demko, and Bart Geerts[1],

University of Wyoming

Second revision

Mon. Wea. Rev.,

7 April 2010

13 Figs, of which 8 in color

[1] *Corresponding author address*: Bart Geerts, Department of Atmospheric Sciences, University of Wyoming, Laramie WY 82071, USA; email: geerts@uwyo.edu

A numerical study of the evolving convective boundary layer and orographic circulation around the Santa Catalina Mountains in Arizona. Part II: Interaction with deep convection

Abstract

This is the second part of a study that examines the daytime evolution of the thermally-forced boundary-layer (BL) circulation over a relatively isolated mountain, about 30 km in diameter and 2 km high, and its interaction with locally-initiated deep convection, by means of numerical simulations validated with data collected in the 2006 Cumulus Photogrammetric, In situ and Doppler Observations (CuPIDO) field campaign in southeastern Arizona. Part I examined the BL circulation in cases with at most rather shallow orographic cumulus convection; the present part addresses deep convection. The results are based on output from the Weather, Research and Forecasting v.3 model run at a horizontal resolution of 1 km. The model output verifies well against CuPIDO observations.

In the absence of Cu convection, the thermally-forced (solenoidal) circulation is largely contained within the BL over the mountain. Thunderstorm development deepens this BL circulation, with inflow over the depth of the BL and outflow in the free troposphere aloft. Primary deep convection results from destabilization over elevated terrain, and tends to be triggered along a convergence line, which arises from the solenoidal circulation but may drift downwind of the terrain crest. While the solenoidal anabatic flow converges moisture over the mountain, it also cools the air. Thus a period of suppressed anabatic flow following a convective episode, at a time when surface heating is still intense, can trigger new and possibly deeper convection. The growth of deep convection may require enhanced convergent flow in the BL, but this is less apparent in the mountain-scale surface flow signal than the decay of orographic convection. A budget study over the mountain suggests that the precipitation efficiency of the afternoon convection is quite low, ~10 % in this case.

1. Introduction

This is the second of a two-part paper that examines the daytime evolution of the thermally-forced boundary-layer (BL) circulation over an isolated mountain, about 30 km in diameter and 2 km high, and the interaction of this circulation with orographic cumulus convection. In Part I (Demko and Geerts 2010, hereafter referred to as DG10), two cases were presented: one was cloud-free, and the second produced orographic convection just deep enough to yield a trace of precipitation. In the present study, a third case is analyzed, in which isolated, deep, precipitating convection developed over the mountain.

Most of the warm-season precipitation in arid mountainous regions results from deep convection that is triggered over the mountains (e.g., Banta and Schaaf 1987; Gochis et al. 2004). This study is motivated by the importance of this deep convection to warm-season precipitation and the importance of mountains as a conduit of surface-BL-troposphere exchanges of water and heat. Because the BL depth and circulations in complex terrain are inadequately represented by numerical weather prediction (NWP) models, the predictability of this precipitation is relatively poor (e.g., Giorgi 1991; Bright and Mullen 2002). The poor predictability is only in part due to the small size of the mountains over which thunderstorms form, compared to the resolution of current-generation NWP models (e.g., Yuan et al. 2007). Yet even NWP model simulations of sufficient resolution to resolve the thermally-direct orographic circulations are challenged in their ability to simulate the surface fluxes and convective BL (CBL) growth over complex terrain, and thus to accurately predict the timing and intensity of the first orographic thunderstorms (e.g., Walser and Schär 2004; Li et al. 2004; Hohenegger and Schär 2007). Such accurate prediction is important because the energy released in a thunderstorm is far greater than that associated with the orographic BL circulation, and thus primary convective initiation drives subsequent deep convection, including mesoscale convective systems (e.g., Wandishin et al. 2008), which may develop in the evening during the Arizona monsoon (e.g., McCollum et al. 1995; Damiani et al. 2008).

This study focuses on the Santa Catalina Mountains (CM) in Arizona, the target area of the Cumulus Photogrammetric, In situ and Doppler Observations (CuPIDO) experiment in July and August 2006 (Damiani et al. 2008). On most days during CuPIDO a deep, weakly capped CBL developed, and tropospheric winds were weak. This study mainly employs output from the Weather, Research and Forecasting (WRF) v.3 model (Skamarock et al. 2008). The simulations compare favorably with CuPIDO observations for the two case studies in DG10.

This modeling study builds on an observational study (Demko et al. 2009), which uses CuPIDO data in order to document a toroidal heat-island circulation within the CBL, centered at the mountain. Data from ten surface stations, positioned around the mountain, clearly demonstrate the diurnal cycle of mountain-scale convergence (MSC), peaking close to local solar noon. On days without deep convection, the daytime evolution of this surface MSC is rather unperturbed and is in sync with the anabatic horizontal pressure gradient force (Geerts et al. 2008). On days with deep convection in the afternoon, the surface flow around the CM tends to temporarily become divergent following a convective outbreak, due to cold-pool spreading (Geerts et al. 2008; Demko et al. 2009). Yet CuPIDO observations do not clearly reveal the solenoidal *forcing* (i.e., a warm anomaly in the CBL over the mountain) or the full solenoidal circulation (with divergent flow near the CBL top). Moreover, observations fail to capture any enhanced MSC near the surface preceding vertical growth spurts of orographic convection (Demko et al. 2009).

The WRF simulations for the two cases presented in DG10 do reveal a warm anomaly over the high terrain during the day. On both days this anomaly is rather shallow and does not extend over the depth of the CBL, which bulges over the mountain. They also reveal a solenoidal circulation with divergent flow mostly contained within the CBL, but even in the model output this circulation and especially its upper-level return flow branch are difficult to capture, since they are overwhelmed by thermals. Regarding the effect of moist convection, the simulations for the 2nd case in DG10 show that

relatively shallow cumulus convection can temporarily overwhelm surface MSC by cloud shading and convective downdraft dynamics.

The objective of Part II is to use the dynamically consistent, continuous WRF model output for a CuPIDO case to shed light upon how the convergent BL circulation affects the initiation and evolution of orographic thunderstorms, and how deep convection affects the BL circulation. The same analysis method as in DG10 is used, and a distinction will be made between an early period with mediocre convection and a later period with cumulonimbus development. The horizontal and vertical fluxes of mass, sensible heat, and vapor in/out the CBL and free troposphere over the mountain will be examined and contrasted with the dry case in DG10.

The remainder of this paper is organized as follows: Section 2 compares the WRF-simulated with the observed evolution of the CBL circulation and convection for this CuPIDO case. Section 3 uses model output to examine the interaction between CBL circulation and deep convection. The budgets of mass, heat and moisture over the mountain are discussed in Section 4. Section 5 discusses the key results and Section 6 lists the conclusions.

2. Model validation

This paper focuses on daytime convective development on 6 August 2006, which was chosen for several reasons. Firstly, isolated orographic cumulus grew into cumulonimbus clouds over the CM without much interaction with convection developing over mountains in the vicinity. Secondly, the deep-layer mean wind (3 m s^{-1} from the east) and wind shear were relatively weak. And thirdly, the convective available potential energy (CAPE) was relatively low, such that deep convection remained mostly confined to the mountains. In several other CuPIDO cases, deep convection broke out over the mountain and soon thereafter over the surrounding valleys, such that it became impossible to discern the orographic BL circulation.

The WRF Nonhydrostatic Mesoscale Model (WRF-NMM) version 3.0.1.1 is used, with initial and boundary conditions determined by the 12 km NAM (North American Mesoscale) grids. The model is initialized at 00 UTC (i.e., the evening before), and the model forecast for 06 to 30 hours is analyzed. Three nested domains are used (Fig. 1 in DG10), with two-way interaction between domains. Cumulus convection is resolved in the middle and inner domains. Here we only examine output from the inner domain, a 103x103 km^2 with a resolution of 1.0 km. The simulations analyzed here use the Mellor-Yamada-Janjić PBL scheme (Janjić 1996) with a Eta similarity parameterization for the surface layer, the Noah Land Surface model (Ek et al. 2003), and the Lin et al. (1983) bulk microphysics scheme. The model output includes a variable called planetary BL (PBL) depth, which is displayed in several figures below. For more information about numerical model setup and sensitivity tests, the reader is referred to DG10.

a. Sounding data and cumulus evolution

The Tucson (KTUS) 12 UTC (pre-dawn) sounding reveals several stable layers below 500 hPa, the strongest ones around 780 hPa, or slightly below the level of Mt. Lemmon [the peak of the CM at an elevation of 2791 m (~ 730 hPa)] and around 550 hPa (**Fig. 1**a). Pre-dawn winds were very weak (<5 kts) below mountain top level; weak easterly flow was present between 700-600 hPa, and stronger southwesterly flow above 450 hPa, up to the tropopause. Weak winds persisted during the day (**Fig. 2**), mostly <10 kts (south)easterly winds below 400 hPa and slightly stronger (<15 kts) southwesterly winds above 400 hPa, according to the four Mobile GPS Advanced Upper-Air Soundings (MGAUS) collected on 6 August. The MGAUS sondes were released from Stratton Canyon located 12 km ENE of Mt Lemmon (**Fig. 3**). The location was selected because the mean wind in the cumulus layer was expected to carry convection to the west, which it did. So the MGAUS profiles represent conditions close to the mountain, but hardly affected by orographic convection.

The 12 UTC WRF sounding at the location of KTUS does not reveal the multiple low-level stable layers, and it overestimates the 700-600 hPa easterly jet (Fig. 1). By the time of first cumulus convection over the CM, the model profiles are closer to the observed (MGAUS) profiles (Fig. 2). The model nicely captures the upstream wind profile during the period of convective growth (18-21 UTC). It underestimates the BL temperature at 1931 UTC (local solar noon), but overestimates it at 2100 UTC (Fig. 2). The BL water vapor mixing ratio was estimated accurately at 1752 UTC, but underestimated in the model by 2-3 g kg^{-1} at 1931 and 2100 UTC. Apparently humidity increased in Stratton Canyon between the three MGAUS sounding times. This is confirmed by data from an Integrated Surface Flux Facility (ISFF) in the canyon. Much of this humidity increase appears to be due to high local evaporation from a nearly saturated soil (not shown). WRF also increases the surface (2 m) mixing ratio, mainly on the northern periphery of the mountain (as observed), but less rapidly and ~2 hours earlier than observed. Stratton Canyon had received much precipitation in previous days. This precipitation was highly heterogeneous in coverage. All nine other ISFF stations around the mountain reported a lower mixing ratio between 18-23 UTC than at Stratton Canyon, up to 7 g kg^{-1} lower. Thus the MGAUS soundings may overestimate the BL moisture over the CM, and the WRF soundings in fact may be more representative. As a result, the observed convection topped well below the equilibrium level (EL) in the last three MGAUS soundings. For instance, the 1931 UTC sounding has an EL of 16.5 km (Fig. 2b), whereas the highest Cu cloud top observed on this day merely reached 9.4 km MSL (**Fig. 4a**). The MGAUS CAPE values[2] are 2-3 higher than CAPE values in the corresponding WRF soundings (Fig. 4a). Note that WRF uses the Noah Land Surface model with initial soil moisture provided by the 12 km NAM model.

[2] The computation of the observed CAPE and CIN required some interpolation because there were gaps in the MGAUS data, as can be seen in Fig. 2. CAPE was computed from the MGAUS and model profiles assuming a 50 mb deep mixed boundary layer. This computation includes the virtual temperature correction. The model stability parameters were computed for each grid point in the 30x30 km^2 box shown in Fig. 3, and then averaged.

The model overestimates the humidity above 550 hPa at all times, and it misses a persistent stable layer around 540 hPa (Fig. 2). Both the stable layer and low humidity aloft probably can be attributed to subsidence, which the model apparently fails to capture. This may be one reason why cumulus convection over the CM grows deeper in the model than in reality (Fig. 4a). Another reason why the modeled convection reaches heights closer to the model EL is that erosive effect of entrainment is captured inadequately in the 1 km simulation. A sensitivity run with an inner domain at 0.5 km horizontal resolution and twice as many levels in the vertical decreases the maximum cloud top at all times (except at the earliest time, 18 UTC), by 0.8 km on average, but otherwise shows a similar convective evolution compared to the control run. The cloud top evolution shown in Fig. 4a is inferred from stereo-photogrammetry (Zehnder et al. 2007), using two cameras located some 40 km southwest of Mt Lemmon (Damiani et al. 2008).

Cumulus clouds first appeared over the CM at 1840 UTC. They quickly grew to become Cu congestus; a maximum cloud top of 9.4 km MSL was reached at 2100 UTC (Fig. 4a). No lightning was recorded over the CM. The 1931 and 2100 UTC MGAUS soundings reveal virtually no convective inhibition (CIN), although in areas away from Stratton Canyon and the CM there probably was some CIN, as suggested by the lack of convection in the San Pedro and Tucson valleys (Fig. 3). The first orographic cu developed over the highest ridges (Fig. 4b). Later the deepest convection occurred further upstream, near the eastern fringes of the CM. Camera animations show that individual cumulus clouds over the CM hardly drifted. Initially clouds slowly moved westward, after 22 UTC they drifted eastward. Although no precipitation was recorded at any of the ISFF stations nor at Mt. Bigelow station, at nearly the same elevation as Mt Lemmon (locations shown in Fig. 3), the camera footage reveals virga down to the mountain surface, mainly at 21 UTC.

The model generates some CAPE over the CM, beginning at 16 UTC and increasing to nearly 400 J kg^{-1} three hours later (Fig. 4a). Model CAPE decreases between 19-21 UTC as non-precipitating convection develops, and then increases again to ~500 J kg^{-1}. This value is small compared to typical

CAPE values near air mass thunderstorm, but the 30 x 30 km^2 box-average CAPE values underestimate model CAPE values closer to Mt. Lemmon. Without substantial CIN, these CAPE values appear to suffice for deep, precipitating convection (topping at 11 km MSL) to develop around 23 UTC (Fig. 4b).

b. Surface measurements

The diurnal surface temperature trend observed at the ten ISFF stations located in the foothills around the mountain is captured rather well by WRF. The main exception is an unobserved, short-lived ~5 K cooling in most quadrants around the mountain stations 23 to 00 UTC (**Fig. 5**a and b), as deep convection matures over the CM in the model (Fig. 4), resulting in a cold pool with divergent surface flow around the mountain (Fig. 5c). The model PBL top is above the CM top for much of the day, 18-23 UTC (Fig. 4a). The modeled excess potential temperature at Mt Bigelow over the foothill stations during this period (Fig. 5b) is indicative of solenoidal forcing for a toroidal BL circulation centered over the CM. The observed potential temperature excess at Mt Bigelow between 18-23 UTC is smaller. This may be due to cloud shading and cold pool dynamics from orographic cumuli, which peaked earlier (between 20-22 UTC) than in the model (Fig. 4a).

The surface component of the solenoidal flow is best estimated in terms of MSC (Demko et al. 2009). The MSC shown in Fig. 5c is calculated as the line integral of the surface wind normal to a closed loop around the CM, divided by the area contained within the loop. In the case of ISFF measurements, the loop is a 576 km^2 decagon (Demko et al. 2009). For validation purposes we mine model output for the same decagon (Fig. 5c). Further model output analysis in this paper uses a more rigorous estimate of MSC, based on a 30x30 km^2 box centered on Mt Lemmon (Fig. 3), with 120 points (since the model resolution is 1 km) vs. 10 data points (i.e., 10 stations). The MSC within this square is also shown in Fig. 5c. The modeled nocturnal surface katabatic flow is stronger than observed, but the magnitude of the modeled daytime 10-point MSC matches observations, with net

convergence starting between 14-15 UTC, as observed. The period of convective deepening (22-23 UTC, Fig. 4a) corresponds with enhanced surface MSC in the model (Fig. 5c). In reality the deepest convection occurred earlier (Fig. 4a), and its decay is evident in weak mountain-scale surface divergence around 22 UTC (Fig. 5c).

In addition to surface potential temperature and MSC, we evaluate the horizontal pressure difference between any of the 10 ISFF stations and the mountain top (Fig. 5d and e). This pressure difference is based on the station pressure data, with the 24 hour mean at any station and the residual 11-station mean at any given time removed. It also includes a correction for the diurnal temperature and pressure cycles, following Geerts et al. (2008). Observations (Geerts et al. 2008) and WRF simulations for two dry cases (DG10) indicate that the horizontal pressure difference typically is negative at night, peaking near sunrise, and typically becomes positive (implying anabatic wind forcing) a few hours after sunrise, peaking in the early afternoon. The 6 August model horizontal pressure difference follows this trend, and becomes positive in the morning about 1 hr earlier than observed (Fig. 5d and e). Its afternoon maximum is close to the observed value, suggesting that WRF accurately captures the lower tropospheric temperature variation around the CM (since these pressure variations are largely hydrostatic). The convectively-induced cold pool produces a dip in anabatic wind forcing at 00 UTC (higher pressure over the CM). There is a few hours lag between the MSC (Fig. 5c) and the anabatic forcing, which peaks near 23 UTC according to observations (Fig. 5d) and at 22 UTC in the model (Fig. 5e). This lag will be revisited later.

3. WRF evolution of the boundary layer and orographic convection

a. Surface conditions

We now use WRF model output to examine the evolution of the BL flow and its interaction with orographic convection (**Figs. 6** and **7**). At 12 UTC, 30 min before sunrise, drainage flow is simulated in valleys within the CM range, spreading over the adjacent broad valleys to the west and

east of the CM. The potential temperature map (Fig. 6a) matches the terrain map (Fig. 3). Anabatic flow is first evident at 15 UTC, mainly on the east side of the CM, as the deepening CBL ingests some easterly momentum from higher levels (Fig. 2). By 19 UTC the CM is well within the CBL (Fig. 4a), but the elevated terrain retains a higher surface θ than the surrounding lowlands. During much of the day and mainly between 18-21 UTC, the CBL θ is higher, and the CBL deeper, in the San Pedro valley to the east of the CM (Fig. 3), compared to the Tucson valley to the west. This pattern is recurrent in WRF simulations, including the two cases in DG10. Unlike most other days, the ISFF observations do not confirm such east-west difference on 6 August (Fig. 5a), probably because much rain had fallen on the east side of the CM during the previous days.

A sinuous meridional convergence line can be seen over the CM starting at 16 UTC, prior to moist convection (dashed blue line in **Fig. 8**a). This boundary results from the confluence of anabatic flow from opposite sides of the CM spine, which is roughly N-S oriented (Fig. 3). It is best defined at 18 UTC (Fig. 6c and Fig. 8c), with cumulus developing above. Mainly the southern half of this boundary slowly propagates westward in the early afternoon, not by solenoidal forcing (the higher temperature on the east would result in eastward propagation), but because of the prevailing easterly flow (Fig. 2, Fig. 6). Convective initiation along a convergence line drifting downwind from the crest has been observed elsewhere (e.g., Banta 1984). Cumulus develops along this boundary through 00 UTC, mainly over the highest terrain, esp. near Pusch Ridge (Fig. 3), where persistent convergent flow leads to increasingly deep convection (Fig. 8c-f). The boundary becomes less-defined as a result of convective outflows (Fig. 8d and e).

Surface MSC over the CM increases steadily until 18 UTC (Fig. 5c). It decreases slightly as rather shallow convection develops and matures between 19-21 UTC, but over a broader scale (e.g., in a 40x40 km^2 square around the CM) it continues to increase until the effects of deeper convection peaking at 00 UTC are felt (not shown). Orographic Cu continue to deepen (Fig. 4a) with a trace of

precipitation first falling at 21 UTC over Pusch Ridge and near Mt Lemmon (Fig. 6f). The cooling (locally up to 4 K) due to cloud shading, the evaporation of rain, and the downward transport of low θ_e results in a decrease in MSC at this time (Fig. 5c). Convection is suppressed during the next hour (Fig. 4a) and no precipitation occurs (Fig. 7a). This evolution is similar to the 9 July 2006 case analyzed in DG10.

But unlike the 9 July case, new Cu develop over the CM at 22 UTC as the cold pools are advected off the mountain and warm air re-establishes over the highest terrain (Fig. 7a). As a consequence, a sharp increase of MSC occurs between 21-23 UTC (Fig. 5c). Specifically, a cell of deep convection develops just north of Pusch Ridge (Fig. 7b). Precipitating convection also develops in the San Pedro Valley during this period, still well within the model's inner domain.

Convective evolution over the CM becomes rather complex at 23-00 UTC, with secondary convective initiation due to outflow boundaries colliding with the terrain, with another outflow boundary, or with channels of upslope flow. For instance, the outflow from the Pusch Ridge cell produces a secondary cell over Bear Canyon (see Fig. 3), yielding the deepest tower of the day, at 00 UTC. Most precipitation accumulated on this day falls from these two cells, with a maximum of 14 mm/hour (Fig. 7c). This complex outbreak of deep convection results in divergent surface flow around the CM, starting at 00 UTC and continuing into the night (Fig. 5c). Weak anabatic forcing is restored for a few hours (Fig. 5e), but it does not result in net convergent flow at the surface. At 01 UTC, only anvils remain over the mountain footprint and precipitation ends (Fig. 7d).

b. Solenoidal circulation and its forcing

In DG10 we argued that some temporal or spatial averaging is needed to isolate the solenoidal forcing and the resulting circulation in the BL. In order to retain good temporal resolution in an east-west cross section, we average across 21 km in the north-south direction, which corresponds with the

long axis of the CM chain (Fig. 3), and is normal to the prevailing wind (Fig. 2). Because the San Pedro valley to the east becomes warmer than the Tucson valley to the west during the day (Fig. 6), we remove the mean potential temperature on each side of the mountain ($\overline{\theta_{east}}$ and $\overline{\theta_{west}}$ respectively) at any pressure level, and plot the residual anomalies (θ'). The vertical profiles of $\overline{\theta_{east}}$ and $\overline{\theta_{west}}$ are show in a side panel in **Fig. 9**. The departure (u') from the mean zonal wind across the entire length of the cross section ($\bar{u}$) is contoured in Fig. 9. The profile of $\bar{u}$ is shown in the right side panel in Fig. 9.

The pre-dawn hours (12 UTC) witness shallow drainage flow with a peak magnitude of 3 m s^{-1} on both sides. The easterly stratified flow aloft accelerates slightly just downstream of the mountain and experiences some lee wave motion. Shallow anabatic flow, approximately 1 m s^{-1} in strength, develops by 15 UTC (Fig. 9b). This is in response to a shallow warm anomaly, initially just on the eastern slopes, but by 17 UTC more uniformly distributed across the mountain, and over a depth corresponding to that of the anabatic circulation.

By 18 UTC (Fig. 9c), the time that the first orographic Cu appear in the WRF simulation, the PBL has deepened, esp. over the San Pedro valley and over the CM, and vertical velocities in the CBL have increased. An updraft peaking at 0.8 m s^{-1} is found just west of the mountain. This updraft is coincident with the convergence line mentioned before (Fig. 8c). The anabatic circulation has strengthened to 2 m s^{-1} on both sides and has deepened to encompass the lower half of the CBL. In the upper CBL weak divergent flow (~1 m s^{-1}) and a cold anomaly have developed, consistent with the two cases in DG10.

At 21 UTC, three updraft regions exist (Fig. 9d). The westernmost one is the deepest and strongest (0.8 m s^{-1}), and roughly corresponds with the convergence line in Fig. 8f. It is coincident with the deep convergence of anabatic flow (~2 m s^{-1} in strength) from the west and the east, the latter spilling over the high ridge due to prevailing easterly flow. The warm anomaly is ~1 km deep (comparable to the depth of the anabatic flow),~15 km wide and 1-1.5 K strong, which makes this case

similar to the Cu congestus case (9 July) presented in DG10. Very weak return (divergent) flow exists above the warm anomaly, and is still largely contained within the CBL. The strength and depth of the low-level anabatic flow (compared to the return flow) suggests that at this time BL air is transported into the free atmosphere above the PBL. This will be examined in more detail later. Cross sections for later times (23-00 UTC) are not shown in Fig. 9, because by then deep convection has developed, with convectively induced cold pools and convergence zones, and updrafts whose maxima are above the top of the display in Fig. 9.

c. Mountain-scale convergence and its forcing

To examine the vertical profile of convergence at the scale of the mountain, we use the 30x30 km^2 box centered on Mt. Lemmon shown in Fig. 3. This box encompasses the majority of the CM and generally does not intersect high terrain. Other boxes with the same center have been examined as well, from 10x10 km^2 to 40x40 km^2, but we only show the 30 km dimension because the results from other boxes are not fundamentally different, and because 30 km is a representative diameter of the CM. Also, the 30x30 km^2 encapsulates the drifting convergence line (mentioned in Section 3.a) during its lifetime, whereas the smaller boxes do not. Note that the *surface* MSC (based on 10 m winds) is not computed at a constant pressure level, but rather along the undulating terrain of the box perimeter. In **Fig. 10**, the surface MSC is assigned an altitude corresponding with the average surface pressure along this perimeter. Constant-pressure MSC values are only available above the highest terrain elevation along the box perimeter, i.e. at 840 hPa, a level considerably above the mean altitude of the *surface* MSC (895 hPa). Thus Fig. 10 contains no information between 895-840 hPa. Starting at 840 hPa, the vertical resolution is 20 hPa.

The surface flow becomes convergent at 14 UTC, ~ 1.5 hours after sunrise (Fig. 10). The convergent layer deepens at the same rate as the CBL through 17 UTC. Weak divergence near the CBL top develops after 18 UTC, with a level of non-divergence in the upper CBL throughout the afternoon,

until deep convection erupts. The surface flow becomes weakly divergent at 21 UTC, due to cloud shading and cold-pool dynamics associated with Cu congesti. These clouds transport BL air up above the PBL top, with divergence out of the 30x30 km^2 box into the lower free troposphere, up to 520 hPa. Lower-CBL MSC intensifies again between 21-23 UTC, generating a maximum mountain-scale vertical velocity of 0.2 m s^{-1} near the PBL top. This updraft transports CBL air into the free atmosphere over greater depths, up to ~300 hPa. The maturing of deep convection at 00 UTC leads to strong near-surface divergence, resulting in a dipole of extreme values that stands out in the 12 hour long time-height transect of Fig. 10. Near-surface divergence continues into the evening, as convection decays and shallow katabatic flow develops. Convergent flow persists in the residual CBL above the surface stable layer until 6 UTC because the horizontal pressure gradient remains anabatic through 6 UTC, for all points on the perimeter of the 30x30 km^2 box (**Fig. 11**a). In the 6 August case the surface flow becomes divergent 1.5 hours earlier in the afternoon than on the dry day in DG10, on account of the convective outflows. If the deep convection had occurred earlier, anabatic flow likely would have been restored, given the strong anabatic forcing (Fig. 11a).

In the evening the surface flow becomes disconnected from the pressure gradient force, which operates over a greater depth. The horizontal pressure gradient force at the 30x 30 km^2 scale [derived as in DG10] appears largely immune to the convective development simulated for 6 August (Fig. 11a). The effect of deep convection on horizontal pressure variations is more evident at the smaller scale of the convective cold pool, for instance a weak high temporarily forms over Mt Lemmon relative to points along a 10x10 km^2 square at 00 UTC (Fig. 11b). It is also more evident in the ISFF station record for this day (Fig. 5d). Deeper or larger convection is likely to produce a stronger high during its decay phase, thus affecting the pressure gradient pattern more, as observed (Geerts et al. 2008). At smaller scales the extreme pressure differences are smaller but the MSC values generally higher (Fig. 11).

Evening convergence in the residual CBL above a shallow stable layer occurs on all CuPIDO days simulated, including the two cases in DG10. It is stronger then the convergence needed to compensate for the surface katabatic flow. It remains an open question whether or not this elevated MSC can trigger moist convection, and whether such vesperal convective initiation is affected by afternoon convection. On 6 August 2006, no additional convection developed after the afternoon convection ceased at 01 UTC, but vesperal convective initiation over the CM occurred on several other days in CuPIDO.

4. Mass, moisture and heat budget

a. Mass flux

We now examine fluxes in and out of three volumes with fixed horizontal dimensions, i.e. the 30x30 km^2 box, and with variable vertical boundaries: surface to 0.5z_i for volume #1, 0.5z_i to z_i for volume #2, and z_i to the highest cloud top within the box (Fig. 4) for volume #3. Here z_i is the average PBL top within the box. WRF uses a terrain-following vertical coordinate (sigma). Thus the vertical boundaries of the volumes, expressed in terms of sigma levels, do not intersect the terrain (**Fig. 12**d). Using the notation in Skamarock et al. (2008), the air mass continuity equation is:

$$\frac{\partial \mu}{\partial t} = -\nabla_h \cdot (\mu \vec{v}_h) - \frac{\partial \mu \dot{\eta}}{\partial \eta} \qquad (1)$$

where $\mu = p_{hs} - p_{ht}$, the difference in hydrostatic pressure at the surface (p_{hs}) and the top of the model domain (p_{ht}), $\eta = (p_h - p_{ht})/\mu$ is the mass vertical coordinate, p_h is the hydrostatic component of the total air pressure, $\dot{\eta} = D\eta/Dt$ the total derivative of η and thus the "vertical" velocity in this coordinate system, and $\vec{v}_h$ the horizontal velocity vector. We integrate (1) across a volume with area A and vertical bounds η_1 and η_2:

$$\int_{\eta_1}^{\eta_2}\int_A \frac{\partial \mu}{\partial t} dA d\eta = -\int_{\eta_1}^{\eta_2}\int_A \nabla_h \cdot (\mu \vec{v}_h) dA d\eta - \int_A \int_{\eta_1}^{\eta_2} \frac{\partial \mu \dot{\eta}}{\partial \eta} d\eta dA \qquad (2)$$

The use of the divergence theorem and division by the volume $A\Delta\eta$ yields:

$$\frac{\partial \overline{\mu}}{\partial t} = \frac{1}{A\Delta\eta}\int_{\eta_1}^{\eta_2}\left(\oint_s \mu v_n ds\right) d\eta + \frac{1}{A\Delta\eta}\int_A (\mu\dot{\eta})_1 - (\mu\dot{\eta})_2 \, dA \qquad (3)$$

where v_n is the wind component normal to the perimeter *s* of area *A*, positive inward, and the overbar indicates a volume average. The term on the left in (3) is the change in mass within the volume, which is a function of the mean temperature. The first integral term on the right in (3) is the net horizontal mass flux across the lateral boundaries of the volume, and the second integral is the difference between the net vertical mass flux across the lower and upper boundaries. The integrals are computed as summations with Δx=Δy=1 km (120 points along the perimeter of the 30x30 km^2 box) and over a variable number of vertical levels, with linear interpolation at the edges. The flux terms in (3) are then converted to mass fluxes (kg s^{-1}).

The evolution of the horizontal and vertical mass fluxes for the three volumes is shown in Fig. 12 for the 6 August case. To assess the impact of deep convection on these mass fluxes, the same data are shown in Fig. 12 for a case without any orographic Cu convection, 12 July 2006, a typical pre-monsoon day with a deep, weakly-capped PBL bulging over the mountain (see DG10 for details). For this case, and also for the 6 August case before Cu convection occurs in the 30x30 km^2 box, the top of the upper volume (#3) is defined arbitrarily as 750 hPa until 14 UTC (when CBL growth and anabatic flow start) and 400 hPa after 14 UTC.

More mass converges into the lower PBL (*HMF$_1$* – see Fig. 12d for flux labels) and thus more mass is transported into the upper PBL (*VMF$_1$*) on the undisturbed day (12 July) than on 6 August, esp. in the early afternoon (Fig. 12). Thus the orographic solenoidal circulation is stronger on the undisturbed day, and this is not due to a stronger anabatic flow, but rather a deeper CBL: its peak depth

is 1.2 km greater on 12 July. When surface heating makes the air over the elevated terrain anomalously warm (Fig. 9), then the solenoidal circulation within the BL advects cooler air. This tends to lower θ_e and CAPE, or at least prevents CAPE over the mountain to increase much beyond its value in the surrounding plains. Thus the suppressed HMF_1 at 21-22 UTC on 6 August may have been a factor in the rapid increase in CAPE and subsequent convective growth between 21-00 UTC (Fig. 4a).

On 12 July most of the upward transport VMF_1 diverges from the mountain in the upper PBL (HMF_2<0), i.e. much of the solenoidal circulation is contained in the PBL (Fig. 12). On 6 August the upper PBL is *convergent* over the mountain (HMF_2>0) and significant upward transport into the free tropophere (VMF_2) occurs. The latter statement is not precise: the *local* PBL top does not exactly coincide with the average PBL top (z_i) [although it undulates in a similar fashion over terrain as do sigma surfaces (e.g., Fig. 9)], thus VMF_2 is not exactly the flux between the PBL and the free troposphere. As the PBL top bulges more over the mountain than the sigma surfaces on 12 July, VMF_2 is positive on this day as well, at least until the early afternoon. On 6 August VMF_2 grows as convection deepens, between 18-20 UTC and 22-23 UTC (Fig. 4). As convection matures between 23-00 UTC, strong outflow occurs aloft due to anvil formation (HMF_3<0), and as it decays between 00-01 UTC, VMF_2 becomes negative.

A comparison of the deep convection case with the undisturbed case (Fig. 12c) yields the intuitive result that moist convection suppresses the solenoidal PBL circulation (marked by the combination of HMF_1>0 and HMF_2<0) and enhances the transfer of BL air into the free troposphere (VMF_2>0) and away from the mountain (HMF_3<0). This is illustrated further in **Fig. 13** for 23 UTC, the time of Cb outbreak on 6 August[3]. The PBL was deeper on 12 July, yet the mass fluxes generally

[3] It is obvious from Fig. 13 that mass is not precisely conserved in the three volumes. This is partly due to temporal changes in mean density (temperature) within the volume (eqn 3), but mainly because the flow across the volume boundaries is not precisely captured. This is because velocities are staggered one-half grid length from the thermodynamic variables (Skamarock et al. 2008). This offset is especially important in the vertical because the WRF simulation uses only 42 sigma levels and the PBL is a small portion of the model depth. The mass imbalance in any volume is generally less than 10% of the mass fluxes across the volume's boundaries. The differences between the 12 July and 6 August cases are far larger, so the comparisons are meaningful.

smaller at this time. Orographic convection is fed by inflow not only from the lower PBL, but also from the upper PBL, and it disperses the BL air aloft. Thus the effect of deep orographic convection is to expand the vertical scale of the solenoidal circulation over the mountain from the boundary layer to the troposphere.

The changes in mass flux between the BL and the free troposphere can be attributed more directly to deep convection in a comparison between the default WRF run and a run in which all cloud processes are turned off for the 6 August case. In the no_microphysics run the cloud microphysical, dynamical and radiative effects of moist convection are disabled. The differences between these simulations (**Table 1**) obviously are small before convective initiation: for instance, the solenoidal circulation within the CBL is only marginally enhanced in the no_microphysics run between 16-20 UTC (slightly higher z_i, HMF_1, and $|HMF_2|$). The deep convection between 22-00 UTC results in a dramatic increase in mass transport into the CBL over the mountain (HMF_1 and HMF_2), and more transport up into the free troposphere aloft (VMF_2) and away from the mountain ($-HMF_3$). Fluxes are reversed during convective decay at 01 UTC, not just in the PBL but also in the free troposphere. The impact of convection on mass fluxes according to the original vs. no_microphysics runs (Table 1) is generally the same in sign and similar in magnitude to the differences between the 6 August and 12 July cases during the period of deep convection (Fig. 12c).

b. Moisture and heat flux

We now compare heat and water vapor fluxes over the CM for the deep convection case (6 August) against those for the dry case (12 July). These fluxes are defined as follows for a volume with vertical bounds (η_1, η_2) and horizontal area A:

horizontal heat flux (HHF): $$\frac{C_p}{A\Delta\eta}\int_{\eta_1}^{\eta_2}\left(\oint_s \theta\mu v_n ds\right)d\eta$$

horizontal vapor flux (*HVF*): $\frac{1}{A\Delta\eta}\int_{\eta_1}^{\eta_2}\left(\oint_s q_v \mu v_n ds\right)d\eta$

vertical heat flux (*VHF*): $\frac{C_p}{A\Delta\eta}\int_A \theta\mu\dot{\eta}dA$

vertical vapor flux (*VVF*): $\frac{1}{A\Delta\eta}\int_A q_v\mu\dot{\eta}dA$ (4)

where C_p is the specific heat under constant pressure and q_v the specific humidity. The flux terms in (4) are converted to units of W and kg s^{-1} for heat and vapor fluxes, respectively. Neither heat nor water vapor is generally conserved in any volume, and sub-grid-scale eddy fluxes are non-zero, so the net fluxes across the boundaries of a volume are not generally zero even if the mass fluxes balance. **Table 2** summarizes the differences in the horizontal and vertical transport of sensible heat and vapor between the thunderstorm case and the dry case for the two PBL volumes.

Because of a deeper solenoidal circulation (Fig. 12), more sensible heat converges into the lower CBL over the mountain (HHF_1), is carried up (VHF_1), and diverges in the upper CBL (HHF_2) on the dry day (12 July), during 7 hours centered at solar noon. The same applies to water vapor, even though the average mixing ratio was lower on the dry day. The moist convection over the CM on 6 August (18-00 UTC) transports more vapor (VVF_2) and sensible heat (VHF_2) into the free troposphere than on 12 July, and some of this vapor and heat is drawn in from the upper CBL ($HVF_2>0$ and $HHF_2>0$). The outbreak of deep convection on 6 August is responsible for 38 tW of extra heat and nearly 1 kiloton of extra water vapor (98 x 10^4 kg s^{-1}) drawn into the CBL over the mountain (in comparison to the 12 July case; 23-00 UTC data averaged). Most of that extra heat (37 tW) and water vapor (95 x 10^4 kg s^{-1}) is pumped into the free troposphere, where it feeds the convection (Table 2). As convection decays at 01 UTC on 6 August, and convective downdrafts & outflows dominate, the flux differences change sign, and some heat and moisture are returned to the PBL.

The water vapor flux calculations allow an estimation of the average precipitation efficiency over the CM for the 6 August case. Precipitation efficiency (*PE*) is the fraction of all condensed water in a storm that precipitates on the earth surface (e.g., Braham 1952; Auer and Marwitz 1968; Hobbs et al. 1980; Jiang and Smith 2003; Fuhrer and Schär 2005). Practically, we define the *PE* as the ratio of the 30x30 km^2 integrated surface precipitation rate (P_{sfc}) to VVF_2, since the cloud base (LCL) is close to the average PBL top (Fig. 4a). In order to place *PE* in context, we ask what happens to the water vapor drawn into the base of cumulus clouds over the mountain (VVF_2). As a first approximation, for a steady-state storm that remains within the 30x30 km^2 box over the mountain,

$$VVF_2 \approx P_{sfc} + E_{PBL} - HVF_3 + VVF_3 - HIF_3 + \int_{V_3} \rho \Delta q_v dV \quad \text{(kg s}^{-1}\text{)}, \tag{5}$$

where the subscripts refer to the volumes as in Fig. 12d, E_{PBL} is the evaporation of rain below cloud base (specifically, within volumes #1 and #2), and HIF_3 represents the horizontal ice flux owing to anvils spreading outside the 30x30 km^2 box; P_{sfc} is estimated as the average precipitation rate during the past hour. The last term in eqn (5) is the change in storage of water vapor in the upper volume #3 (V_3) by detraining convection, also evaluated over the past hour. A significant fraction of this volume becomes cloudy as deep convection breaks out on 6 August (Fig. 13). Yet this term is insignificant compared to P_{sfc} when the convection is intense. The terms VVF_3 and HIF_3 also prove to be negligibly small during this time. Thus to a first order, precipitation efficiency can be evaluated from:

$$PE - \frac{HVF_3}{VVF_2} + \frac{E_{PBL}}{VVF_2} \approx 1 \tag{6}$$

The model output does not enable a calculation of E_{PBL}, so it is estimated from eqn (5) as the residual term in the water budget. The three ratios in eqn (6) are shown in **Table 3** during the period of precipitation over the CM. The approximate balance of eqn (6) applies within ~20%. During the shallow convective stage (21 and 22 UTC) the majority of the vapor advected into cloud base detrains laterally in the free troposphere (HVF_3<0) or falls as rain but evaporates before reaching the ground

(E_{PBL}). As cumulus deepens over the CM from 22 to 23 UTC (Fig. 4a), most vapor (including the detrained cloud water) is advected away from the mountain, and the precipitation remains very limited: the *PE* does not exceed 1%. It is not until 00 UTC, when most of precipitation occurs (Fig. 7c), that we see an increase in *PE* to 42%, but at this time rain is more likely to evaporate into the PBL (47%) than to reach the ground. On average, over the lifecycle of this orographic convection episode, the *PE* is just 9% and the vapor outflux aloft ($-HVF_3$) is 63%, thus this convection effectively pumps BL water vapor into the free troposphere. We performed sensitivity studies with two other cloud microphysics parameterizations [the Eta scheme and the Thompson et al. (2008) scheme] and obtained similar results (*PE* values of 4% and 12% respectively over the duration of the simulated moist convection), notwithstanding substantially different storm evolutions.

These estimates of *PE* are low compared to that for high-plains thunderstorms [e.g., 55% according to Auer and Marwitz (1968) and 19-47% according to Fankhauser (1988)]. However, a more thorough study of monsoon thunderstorms in China finds that over 90% of the water vapor that enters the clouds through the cloud base detrains in the ambient atmosphere and that less than 10% falls out as surface precipitation (Shusse and Tsuboki 2006). Clearly storm-total *PE* is a function of storm dimensions and surface dewpoint depression. The modeled *PE* cannot be verified because none of the 11 stations reported any precipitation on 6 August and the Tucson S-band radar echoes due to rain cannot be distinguished from ground clutter and biological return.

5. Discussion

An initial burst of Cu congestus growth occurs around local solar noon (19-20 UTC) (Fig. 6d-e) in the WRF simulations for this case (6 August 2006). Since the level of free convection is well below the PBL top over the mountain at this time (Fig. 4a), this Cu development is due to local destabilization, with a CAPE value 260 J kg^{-1} over the mountain (Fig. 4a), rather than being forced by

upslope flow. Cloud shading and convective downdrafts of lower θ_e air suppress the solenoidal forcing (Fig. 6f) and MSC (Fig. 5c) around 21 UTC. This is followed by a new cycle of warming of the CBL over the mountain, an increase in CAPE, and the growth of more numerous and deeper convective towers between 22-00 UTC, culminating in cumulonimbus formation (Fig. 4a, Fig. 7). During this period MSC in the CBL is enhanced to feed the growing convection (Fig. 5c), until convection matures and divergent cold pools form (Fig. 7, Fig. 10).

This case study thus indicates that daytime orographic convection is initiated by local surface heating and destabilization rather than by upslope flow, which reduces CAPE over elevated terrain. A phase of suppressed MSC may increase chances for convective (re)initiation over a mountain. Boundary-layer MSC may increase in response to the growth of sufficiently deep and large convection, before changing sign due to decay of orographic convection. Thus orographic convection differs from convection over flat land, in that the former is initiated by local heating and the latter by BL convergence (e.g., Chapter 5 in Markowski and Richardson 2010). The collapse of convection produces a surface flow signal that is at least as apparent as its growth, consistent with Geerts et al. (2008) and Demko et al. (2009).

It is unlikely that convective conditioning of the environment [i.e., the moisture-convection feedback hypothesis, e.g., Derbyshire et al. (2004); Grabowski and Moncrieff (2004)] explains why the second burst of convection on 6 August is deeper and more intense than the first one. This hypothesis states that convective towers are more resistant to erosion by entrainment in an environment moistened by preceding towers. While moistening does occur in volume #3 (the Cu layer) during both convective bursts, the modeled BL θ_e is higher at the start of the 2nd burst (22 UTC) than at the start of the 1st burst (18 UTC) (not shown), and CAPE is higher during the 2nd burst than the 1st burst (Fig. 4a). Thus changes in the BL are consistent with a relatively deeper 2nd burst of orographic convection. Also, a lull of 1-2 hours exists between the two bursts, which is long enough to advect the moisture in the Cu

layer away from the mountain, notwithstanding the weak winds (Fig. 2). Moreover, at a resolution of 1 km, the WRF-resolved convective towers (e.g., Fig. 13) are unlikely to be much affected by entrainment, as discussed in Section 2a.

6. Conclusions

This paper uses numerical model output to examine how the convective boundary layer over a mountain affects and is affected by locally triggered deep convection. It is based on a case study for a ~30 km wide, ~ 2 km high mountain, in an environment marked by weak winds, weak wind shear, and modest CAPE. It builds on DG10, which uses WRF model output to examine CBL evolution over the same mountain for two others cases, one cloud-free and another with orographic Cu congestus.

Surface, upper-air, and photogrammetric data collected as part of CuPIDO indicate that the model, WRF v.3 with a horizontal resolution of 1 km and 12 km NAM initial fields, reasonably captures the observed temperature distribution, as well as mountain-scale anabatic flow development, the CBL depth, and the stability and wind profiles. Convective growth is delayed a little in the model and the simulated maximum Cu top over the mountain is higher than observed, resulting in more precipitation than observed. These minor disagreements can be attributed at least in part to the absence (in the model) of a mid-level cap and a mid-level dry layer, and an underestimate in local soil moisture. These discrepancies would lessen if CuPIDO field data, such as soundings and surface measurements, had been assimilated into the WRF simulations.

The findings from the present case study corroborate several results in DG10, as follows:

1) Drainage flow transitions shortly after sunrise into anabatic, convergent flow, which peaks close to solar noon.
2) The anabatic flow is forced by a warm anomaly in the lower half of the CBL over the mountain, and thus a horizontal pressure gradient force towards the mountain. The low-level

3) The anabatic pressure gradient forcing persists for some time in the evening, even on a day with afternoon thunderstorms. This forcing results in highly convergent flow in the residual CBL above the drainage flow in a shallow stable layer.

The first two findings corroborate CuPIDO observations (Geerts et al. 2008; Demko et al. 2009). The following additional conclusions can be drawn from the present case study (6 August 2006):

4) In the absence of moist convection, the solenoidal circulation is largely contained within the CBL over the mountain, with low-level convergence and upper-level divergence. Deep convection converts this BL circulation into a tropospheric one, with inflow over the depth of the CBL, mainly the lower CBL, and outflow in the free troposphere aloft.

5) Orographic convection tends to be triggered along a convergence line, which arises from the solenoidal circulation but may drift downwind of the terrain crest. Such a boundary may be long-lived and may be the focus of further convective development as it intersects outflow boundaries or local terrain ridges.

6) Orographic convection is triggered by local destabilization rather than by anabatic flow, which lowers CAPE over the mountain, as it advects colder air. Thus a period of suppressed anabatic flow, e.g. following a first growth phase of orographic Cu convection, can be a precursor for renewed and possibly deeper Cu convection, as long as the surface heating remains intense. This may explain the cyclic nature of daytime convection over a mountain of this size (e.g., Zehnder et al. 2006).

7) Orographic convection in southeastern Arizona does not efficiently produce rain: over the lifetime of the convection, only about 10% of the vertical water vapor flux at cloud base precipitates on the ground. Instead the “sky island” mountains are effective conduits of water vapor from the BL into the free atmosphere.

The ability of WRF v.3 to capture the development of the CBL, the anabatic flow over steep terrain, and the timing and intensity of deep convection at a rather coarse spatial resolution is impressive. Thus we can be optimistic that as the operational WRF model approaches a 1 km resolution in the near future, the predictability of orographic convection and convective precipitation in the Western United States will improve substantially.

Acknowledgements: this research was funded by National Science Foundation (NSF) grants ATM-0444254 and ATM-0849225 and by NSF facility deployment funds. The observed cloud top chronology (shown in Fig. 4) was kindly provided by Joseph A. Zehnder.

References

Auer, A. H., and J. D. Marwitz, 1968: Estimates of air and moisture flux into hailstorms on the high plains. *J. Appl. Meteor*., **7**, 196-198.

Banta, R. M., 1984: Daytime boundary-layer evolution over mountainous terrain. Part I: Observations of the dry circulations. *Mon. Wea. Rev.*, **112**, 340-356.

Banta R. M., and C. L. B. Schaaf, 1987: Thunderstorm genesis zones in the Colorado Rocky Mountains as determined by traceback of geosynchronous satellite images. *Mon. Wea. Rev.*, **115**, 463–476.

Braham, R. R., 1952: The water and energy budgets of the thunderstorm and their relation to thunderstorm development. *J. Meteor*., **9**, 227-242.

Bright, D.R., and S.L. Mullen, 2002: Short-range ensemble forecasts of precipitation during the Southwest Monsoon. *Wea. Forecasting*, **17**, 1080–1100.

Damiani, R., J. Zehnder, B. Geerts, J. Demko, S. Haimov, J. Petti, G.S. Poulos, A. Razdan, J. Hu, M. Leuthold, and J. French, 2008: Cumulus Photogrammetric, In-situ and Doppler Observations: the CuPIDO 2006 experiment. *Bull. Amer. Meteor. Soc.*, **89**, 57–73.

Demko, J. C., B. Geerts, Q. Miao, and J. Zehnder, 2009: Boundary-layer energy transport and cumulus development over a heated mountain: an observational study. *Mon. Wea. Rev. ,* **137**, 447–468.

Demko, J. C., and B. Geerts, 2010: A numerical study of the evolving convective boundary layer and orographic circulation around the Santa Catalina Mountains in Arizona. Part I: Circulation without deep convection. *Mon. Wea. Rev*., accepted.

Derbyshire, S.H., I. Beau, P. Bechtold, J.-Y. Grandpeix, J.-M. Piriou, and J.-L. Redelsperger, 2004: Sensitivity of moist convection to environmental humidity, *Quart. J. Roy. Meteor. Soc*., **130**, 3055 – 3079.

Ek, M. B., K. E. Mitchell, Y. Lin, E. Rogers, P. Grunmann, V. Koren, G. Gayno, and J. D. Tarpley, 2003: Implementation of Noah land surface model advances in the National Centers for

Environmental Prediction operational mesoscale Eta model. *J. Geophys. Res*., 108 (D22), 8851, doi:10.1029/2002JD003296.

Fankhauser, J., 1988: Estimates of thunderstorm precipitation efficiency from field measurements in CCOPE. *Mon. Wea. Rev.*, **116**, 663–684.

Fuhrer, O., and Schär, C., 2005: Embedded cellular convection in moist flow past topography. *J. Atmos. Sci*., **62**, 2810-2828.

Geerts, B., Q. Miao, and J.C. Demko, 2008: Pressure perturbations and upslope flow over a heated, isolated mountain. *Mon. Wea. Rev*., **136**, 4272–4288.

Giorgi F., 1991: Sensitivity of simulated summertime precipitation over the western United States to different physics parameterizations. *Mon. Wea. Rev.*, **119**, 2870–2888.

Gochis, D.J., A. Jimenez, C.J. Watts, J. Garatuza-Payan, and W.J. Shuttleworth, 2004: Analysis of 2002 and 2003 warm-season precipitation from the North American Monsoon Experiment event rain gauge network. *Mon. Wea. Rev.*, **132**, 2938–2953.

Grabowski, W.W., and M.W. Moncrieff, 2004: Moisture-convection feedback in the tropics, 3081 – 3104. *Quart. J. Roy. Meteor. Soc*., **130**, 3081 – 3104.

Hobbs, P. V, T. J. Matejka, P. H. Herzegh, J. D. Locatelli, and R. A. Houze, 1980: The mesoscale and microscale structure and organization of clouds and precipitation in midlatitude cyclones. I: A case study of a cold front. *J. Atmos. Sci.*, **37**, 568-596.

Hohenegger, C., and C. Schär, 2007: Atmospheric predictability at synoptic versus cloud resolving scales. *Bull. Amer. Meteor. Soc*., **88**, 1783–1793.

Janjić, Z. I., 1996: The Mellor–Yamada level 2.5 turbulence closure scheme in the NCEP Eta Model. Research Activities in Atmospheric and Oceanic Modeling, WMO, Geneva, CAS/JSC WGNE, 4.14–4.15. [Available from World Meteorological Organization, Case Postale 2300, CH-1211 Geneva, Switzerland.].

Jiang, Q., and R. B. Smith, 2003: Cloud timescales and orographic precipitation. *J. Atmos. Sci*., **60**, 1543-1559.

Li, J., X. Gao, R.A. Maddox, and S. Sorooshian, 2004: Model study of evolution and diurnal variations of rainfall in the North American Monsoon during June and July 2002. *Mon. Wea. Rev.*, **132**, 2895–2915.

Lin, Y.L., R.D. Farley, and H.D. Orville, 1983: Bulk parameterization of the snow field in a cloud model. *J. Appl. Meteor.*, **22**, 1065–1092.

Markowski, P.M., and Y.P. Richardson 2010: *Mesoscale Meteorology in Midlatitudes*. Wiley, 430 pp.

McCollum, D.M., R.A. Maddox, and K.W. Howard, 1995: Case study of a severe mesoscale convective system in Central Arizona. *Wea. Forecasting*, **10**, 643–665.

Shusse, Y., and K. Tsuboki, 2006: Dimension characteristics and precipitation efficiency of cumulonimbus clouds in the region far south from the Mei-Yu front over the eastern Asian continent. *Mon. Wea. Rev.*, **134**, 1942–1953.

Skamarock, W. C., J. B. Klemp, J. Dudhia, D. O. Gill, D. M. Barker, M. Duda, X.-Y. Huang, W. Wang and J. G. Powers, 2008: A description of the Advanced Research WRF Version 3. NCAR Tech. Note (available at http://www.mmm.ucar.edu/wrf/users/docs/arw_v3.pdf).

Thompson, G., P.R. Field, W.R. Hall, and R.M. Rasmussen, 2008: Explicit forecasts of winter precipitation using an improved bulk microphysics scheme. Part II: Implementation of a new snow parameterization. *Mon. Wea. Rev*., **136**, 5095-5115.

Walser, A., and C. Schär, 2004: Convection-resolving precipitation forecasting and its predictability in Alpine river catchments. *J. Hydrol*., **288**, 57–73.

Wandishin, M.S., D.J. Stensrud, S.L. Mullen, and L.J. Wicker, 2008: On the predictability of mesoscale convective systems: two-dimensional simulations. *Wea. Forecasting*, **23**, 773–785.

Yuan, H., S.L. Mullen, X. Gao, S. Sorooshian, J. Du, and H.M.H. Juang, 2007: Short-range probabilistic quantitative precipitation forecasts over the Southwest United States by the RSM Ensemble System. *Mon. Wea. Rev.*, **135**, 1685–1698.

Zehnder, J.A., L. Zhang, D. Hansford, A. Radzan, N. Selover, and C.M. Brown, 2006: Using digital cloud photogrammetry to characterize the onset and transition from shallow to deep convection over orography. *Mon. Wea. Rev.*, **134**, 2527–2546.

Zehnder, J.A., J. Hu and A. Razdan, 2007: A stereo photogrammetric technique applied to orographic convection. *Mon. Wea. Rev*, **135**, 2265–2277.

Figure captions

Fig. 1: (a) Tucson (KTUS) 12 UTC 6 August 2006 observed (grey lines and symbols) and model (black) soundings on a Stüve diagram, with wind profiles on the right. A full barb corresponds with 5 m s^{-1} (10 kts), and no wind symbol is shown for winds weaker than 1.3 m s^{-1}. (b) Corresponding profiles of potential temperature θ, equivalent potential temperature θ_e, and saturated equivalent potential temperature θ_e^*. KTUS is located 38 km from Mt Lemmon, to the south.

Fig. 2: As Fig. 1b, but the observations (in grey) are MGAUSs at (a) 1752, (b) 1931, and (c) 2100 UTC, released from Stratton Canyon, located 12 km ENE of Mt Lemmon. These are compared with collocated WRF soundings at the closest hour (in black). The vertical line carries θ_e from the most unstable level near the surface upward, indicating the amount of CAPE in the environment.

Fig. 3: Terrain map of the Santa Catalina Mountains, showing the location of the ten ISFF stations, the Mt Bigelow station, the 30x30 km^2 box used for MSC calculations, and several geographic markers.

Fig. 4: Trend of observed vs. modeled orographic cumulus top evolution. Panel (a) shows the trend of various stability parameters and of the highest cloud top and panel (b) maps the location of the highest cloud top. The time resolution is 20 min for the cloud top observations and hourly for the model output. The stability parameters are computed from four MGAUS soundings and from model output averaged within the 30x30 km^2 box shown in Fig. 3. Note: LCL=lifting condensation level; LFC=level of free convection.

Fig. 5: Comparison of observed vs WRF-simulated surface parameters. (a) Observed potential temperature at Mt Bigelow (dashed black line) and at the ISFF stations, color-coded as shown in the insert terrain map; (b) as (a), but from WRF model output; (c) observed (solid black line) and modeled (grey line) surface MSC calculated from the ten ISFF stations, and modeled surface MSC into the 30x30 km^2 box shown in Fig. 3 (dashed line); (d) observed horizontal pressure difference between the ISFF stations and the mountain top [following Geerts et al. (2008), positive values imply a lower pressure over the mountain]; (e) as (d), but from WRF model output. The dark blue ISFF station (Stratton Canyon) was also the MGAUS release site on this day. The vertical dashed lines indicate the times of sunrise, local solar noon (LSN), and sunset.

Fig. 6: Inner-domain maps of 2 m θ (color) draped over the terrain and 10 m winds (thin barbs) for 12, 15, 18-21 UTC on 6 August. Also shown are the 0.01 g kg^{-1} cloud water isosurfaces (transparent) and one-hour accumulated precipitation, with contours of 0.25 mm (white), 2.5 mm (blue), 6.4 mm (light blue), and 12.7 mm (light green).

Fig. 7: As Fig. 6, but for 22-01 UTC.

Fig. 8: Inner-domain maps of 750 hPa vertical velocity (m s^{-1}) and 10 m winds (thin barbs) for 16-21 UTC on 6 August. Also shown are the 0.01 g kg^{-1} cloud water isosurfaces, and elevation contours (black) with an interval of 200 m (labeled in (a)). The black rectangle in the vertical velocity field is due to Mt Lemmon's elevation, slightly above the 750 mb surface. The dashed blue line in each panel highlights a convergence line discussed in the text.

Fig. 9: East-west cross section based on averages computed over 21 km in the north-south direction for (a) 12, (b) 15, (c) 18, and (d) 21 UTC. The white area is the 21-km averaged terrain height. The

cross section shows θ' (color fill), u' (solid black contours for westerly flow and dotted black contours for easterly flow, contour interval 1 m s^{-1}), w (solid grey contours for updrafts and dotted gray contours for downdrafts, contour interval 0.2 m s^{-1}) and PBL height (long-dashed black line). Also shown are profiles of $\overline{\theta_{west}}$ (solid) and $\overline{\theta_{east}}$ (dashed) on the left of each cross section, and $\bar{u}$ on the right. The variables are defined in the text.

Fig. 10: Time-height plot of MSC for the 30x30 km^2 box (color shaded), mountain-scale vertical velocity within this box, inferred from mass continuity (solid lines for updrafts, dotted lines for downdrafts, contour interval 0.05 m s^{-1}), and mean PBL height within the box (bold dashed line).

Fig. 11: (a) Time series of the mean horizontal pressure difference between points along the 30x30 km^2 box and Mt Lemmon (black solid line, left axis), and MSC for the corresponding box (grey lines, right axis), for the 6 August case. The black dotted lines indicate the mean pressure difference ± one standard deviation, based on all grid points of the box's perimeter. A positive pressure difference implies a lower pressure at Mt Lemmon, i.e. anabatic "forcing". Black arrows highlight the times of extreme pressure differences. Grey arrows highlight the same for MSC. The average height of points along the box perimeter is shown in the upper left corner. For comparison, the elevation of Mt Lemmon in the inner WRF domain is 2629 m MSL. (b) As (a), but for a 10x10 km^2 box centered on Mt Lemmon.

Fig. 12: Temporal variation of the horizontal and vertical mass fluxes in/out three 30x30 km^2 volumes, for (a) 6 August (a moist case), (b) 12 July (a dry case), and (c) the difference between the moist case and the dry case. The three volumes are defined in the text and illustrated in (d). Inward and upward fluxes, shown by the arrows in (d), are positive.

Fig. 13: Horizontal and vertical mass fluxes in/out of the three volumes shown in Fig. 12d at 23 UTC for 6 August (a) and 12 July (b). Arrows indicate the direction of flux. Flux quantities are in units of 10^6 kg s^{-1}. The terrain and 0.01 g kg^{-1} cloud isosurfaces are shown as well. The vertical boundaries of the three volumes are shown schematically as flat surfaces; in reality these boundaries are sigma surface undulating with the terrain.

Table captions

Table 1: The *difference* in horizontal and vertical mass fluxes for the three volumes illustrated in Fig. 12d between the original and the no_microphysics WRF simulations, for 6 August 2006. The entire period is broken up in five periods of cumulus evolution. Since $HMF_1 \cong VMF_1$, the average of these two terms is shown as $H(V)MF_1$.

Table 2: The *difference* in horizontal and vertical heat and vapor fluxes for volumes 1 and 2 (illustrated in Fig. 12d) between 6 August and 12 July 2006, based on WRF model output. The bold numbers represent hours with moist convection over the CM on 6 August. Local solar noon at 1929 UTC.

Table 3: Select water fluxes expressed as a percentage of the vertical vapor flux across the PBL top (VVF_2) during the period of precipitation at the surface.

Figures

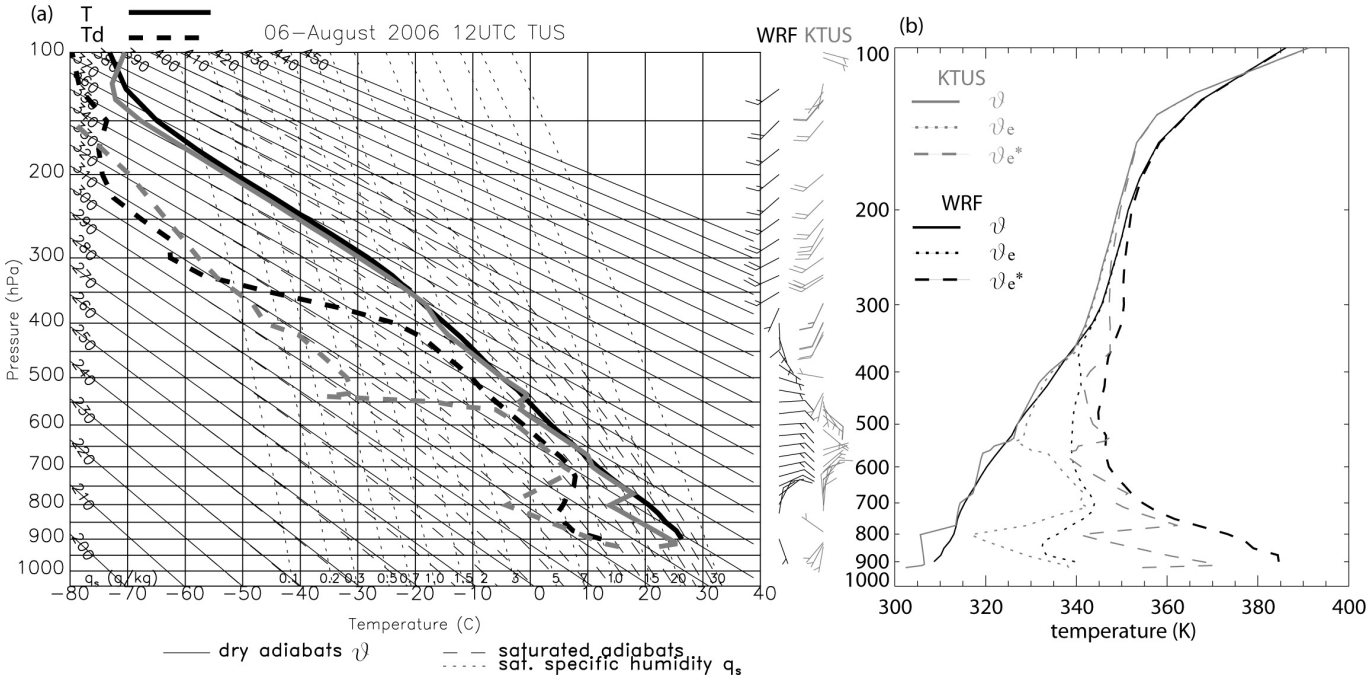

Fig. 1: (a) Tucson (KTUS) 12 UTC 6 August 2006 observed (grey lines and symbols) and model (black) soundings on a Stüve diagram, with wind profiles on the right. A full barb corresponds with 5 m s^{-1} (10 kts), and no wind symbol is shown for winds weaker than 1.3 m s^{-1}. (b) Corresponding profiles of potential temperature θ, equivalent potential temperature θ_e, and saturated equivalent potential temperature θ_e^*. KTUS is located 38 km from Mt Lemmon, to the south.

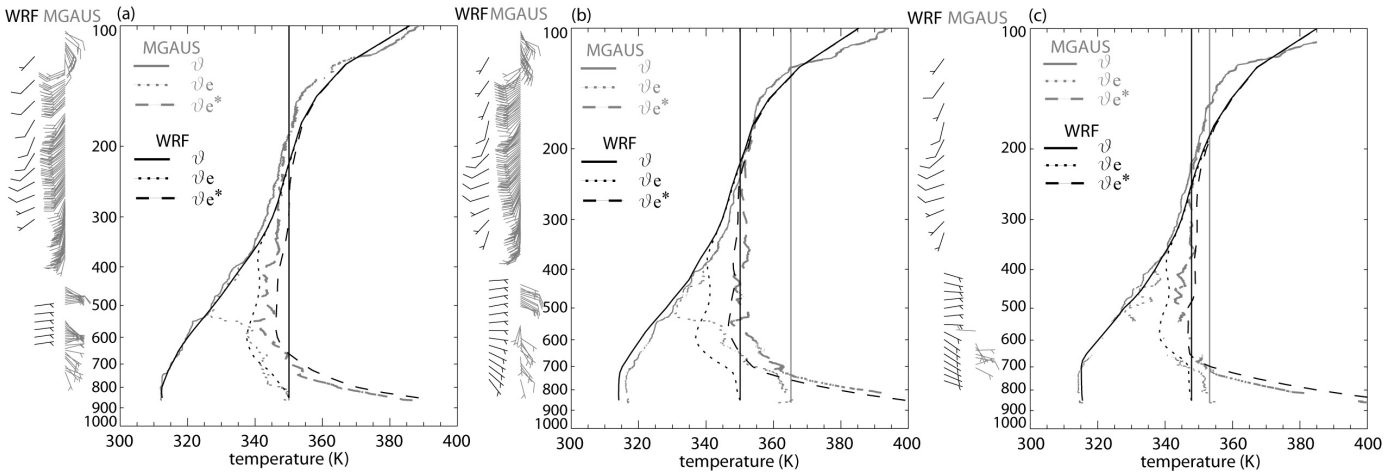

Fig. 2: As Fig. 1b, but the observations (in grey) are MGAUSs at (a) 1752, (b) 1931, and (c) 2100 UTC, released from Stratton Canyon, located 12 km ENE of Mt Lemmon. These are compared with collocated WRF soundings at the closest hour (in black). The vertical line carries θ_e from the most unstable level near the surface upward, indicating the amount of CAPE in the environment.

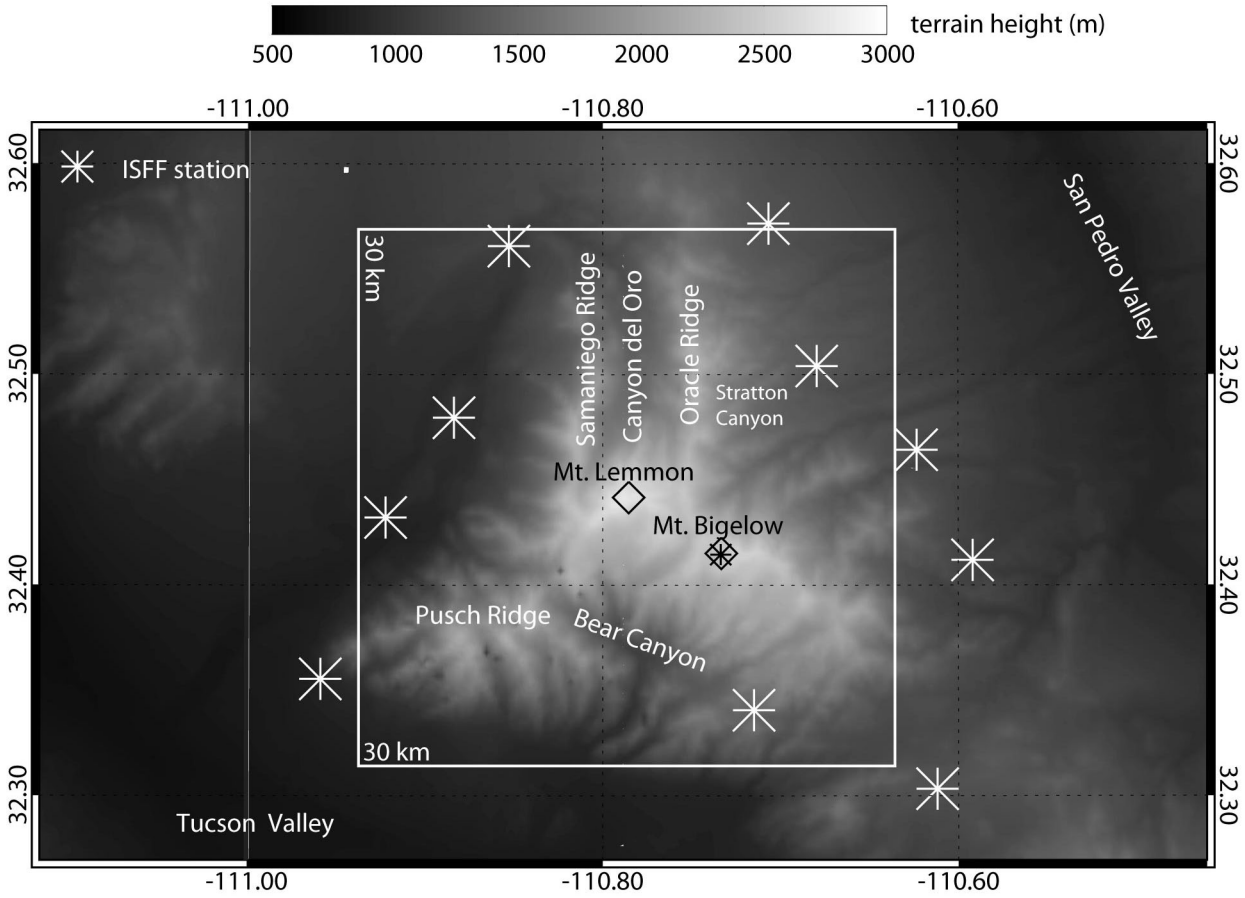

Fig. 3: Terrain map of the Santa Catalina Mountains, showing the location of the ten ISFF stations, the Mt Bigelow station, the 30x30 km^2 box used for MSC calculations, and several geographic markers.

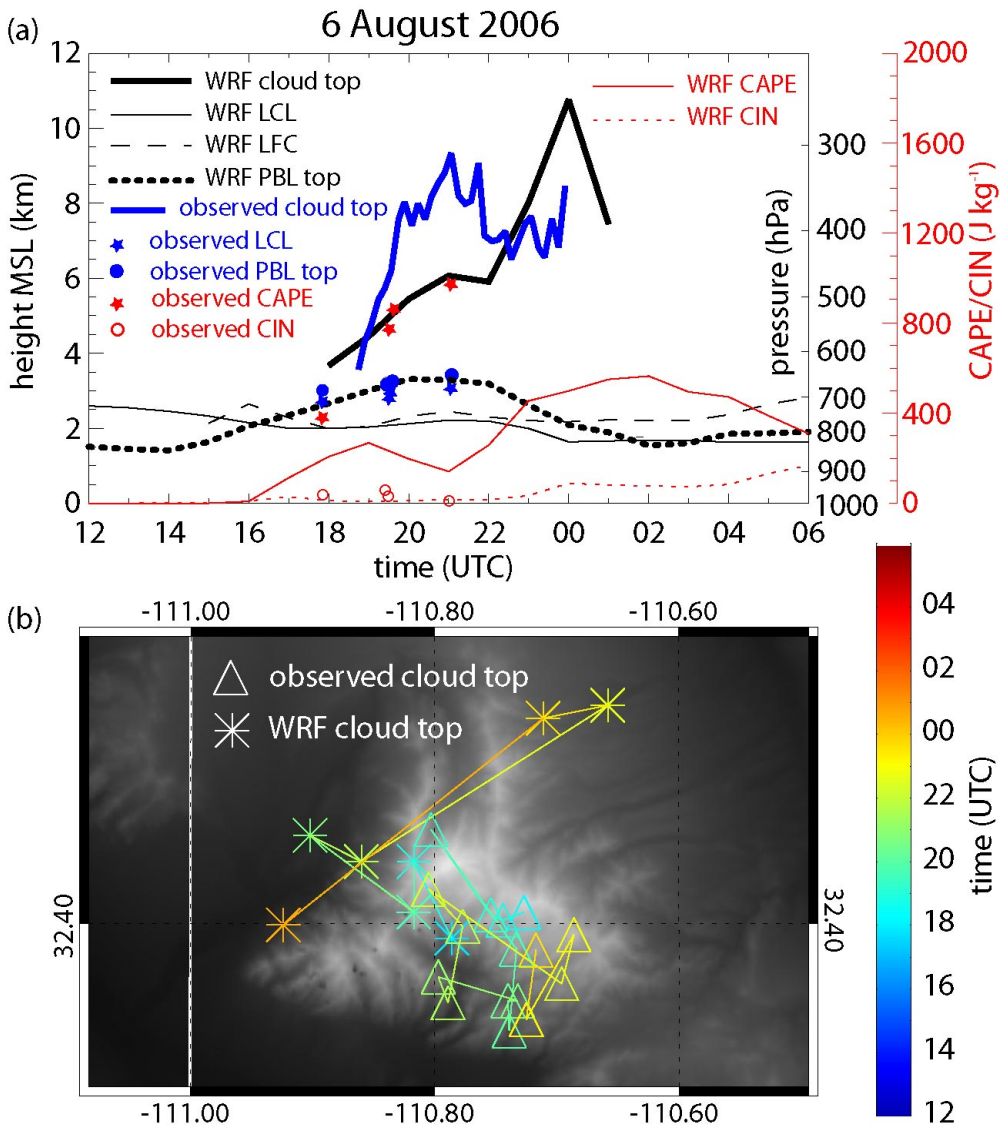

Fig. 4: Trend of observed vs. modeled orographic cumulus top evolution. Panel (a) shows the trend of various stability parameters and of the highest cloud top and panel (b) maps the location of the highest cloud top. The time resolution is 20 min for the cloud top observations and hourly for the model output. The stability parameters are computed from four MGAUS soundings and from model output averaged within the 30x30 km^2 box shown in Fig. 3. Note: LCL=lifting condensation level; LFC=level of free convection.

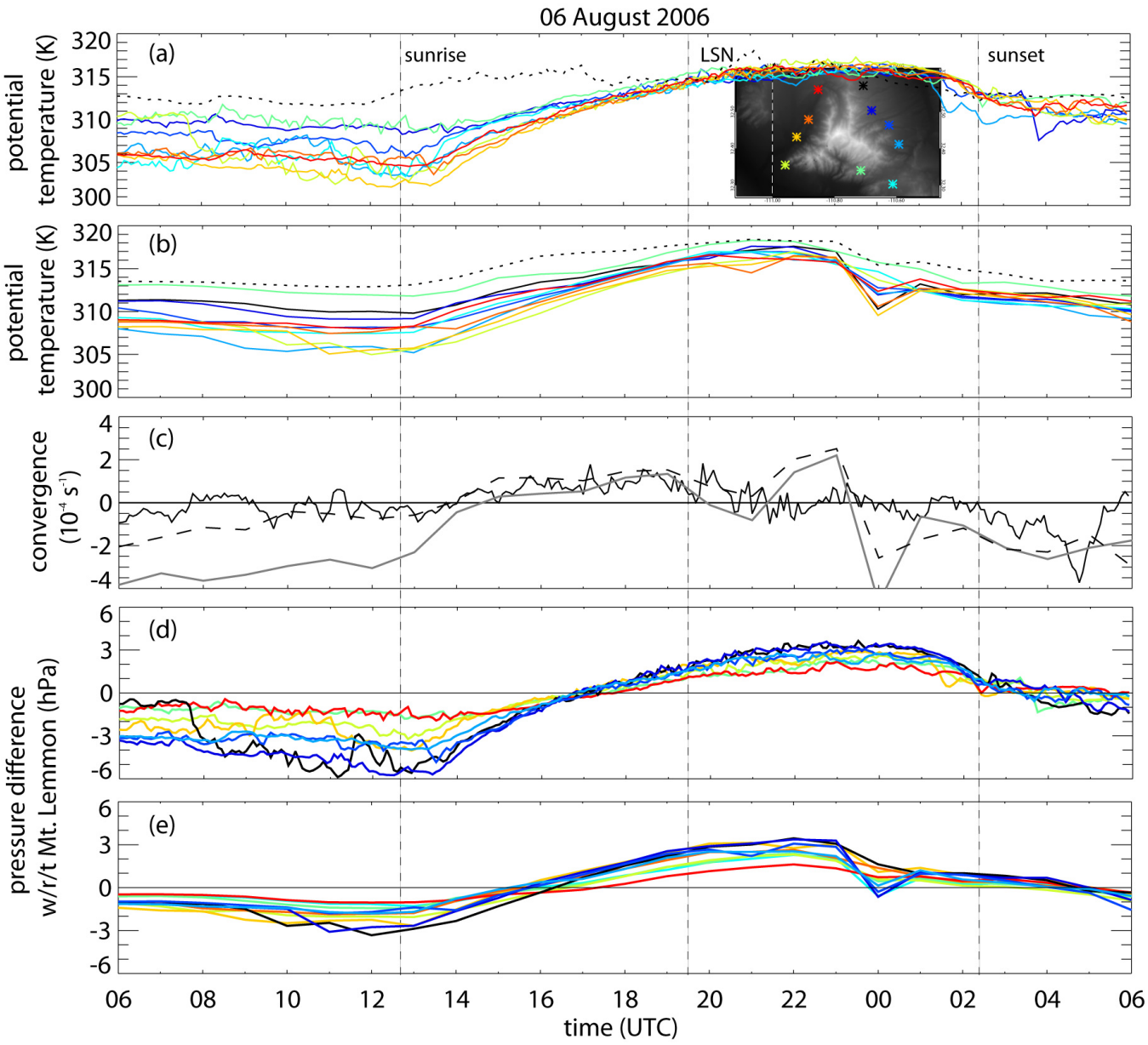

Fig. 5: Comparison of observed vs WRF-simulated surface parameters. (a) Observed potential temperature at Mt Bigelow (dashed black line) and at the ISFF stations, color-coded as shown in the insert terrain map; (b) as (a), but from WRF model output; (c) observed (solid black line) and modeled (grey line) surface MSC calculated from the ten ISFF stations, and modeled surface MSC into the 30x30 km^2 box shown in Fig. 3 (dashed line); (d) observed horizontal pressure difference between the ISFF stations and the mountain top [following Geerts et al. (2008), positive values imply a lower pressure over the mountain]; (e) as (d), but from WRF model output. The dark blue ISFF station (Stratton Canyon) was also the MGAUS release site on this day. The vertical dashed lines indicate the times of sunrise, local solar noon (LSN), and sunset.

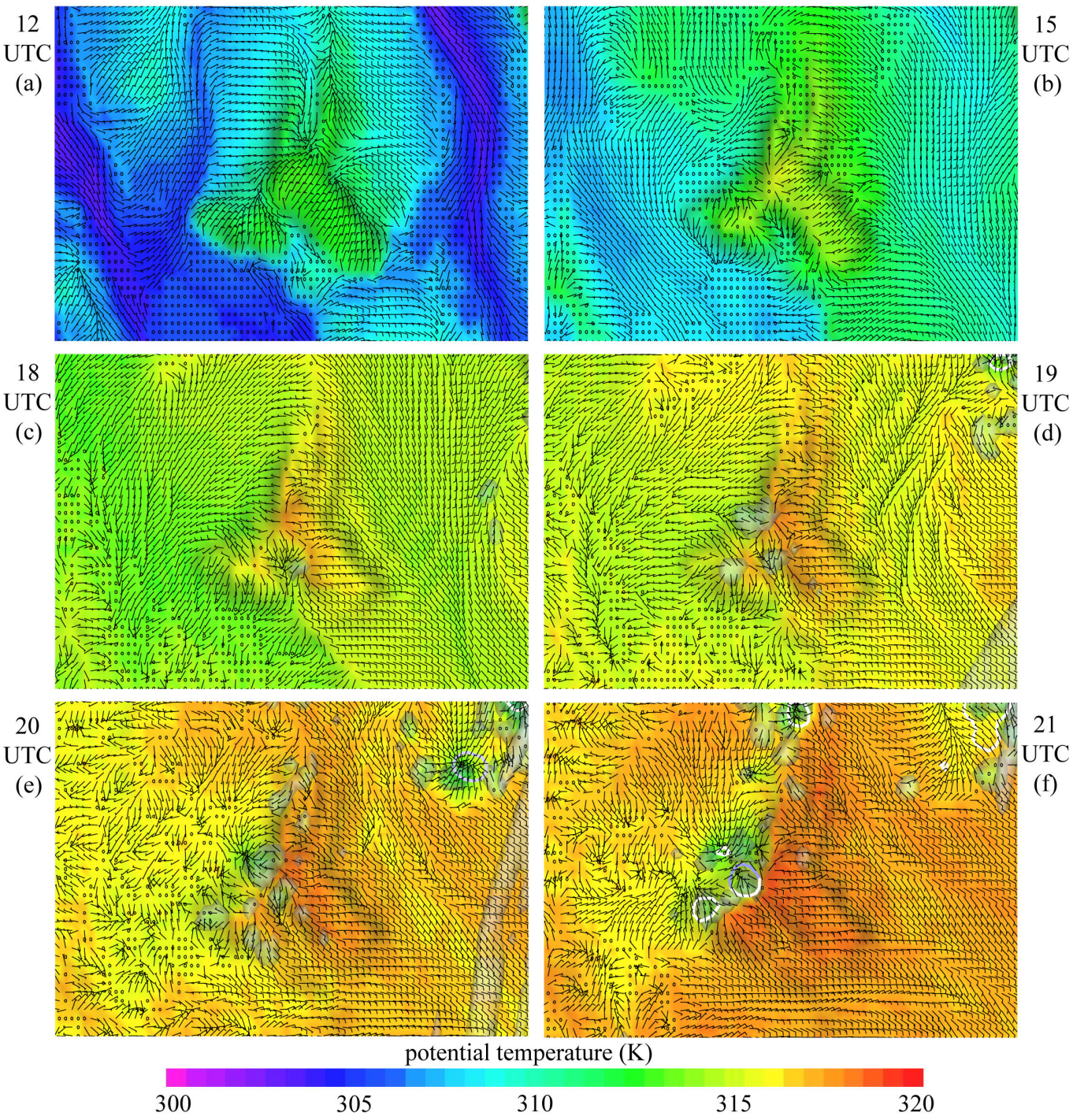

Fig. 6: Inner-domain maps of 2 m θ (color) draped over the terrain and 10 m winds (thin barbs) for 12, 15, 18-21 UTC on 6 August. Also shown are the 0.01 g kg^{-1} cloud water isosurfaces (transparent) and one-hour accumulated precipitation, with contours of 0.25 mm (white), 2.5 mm (blue), 6.4 mm (light blue), and 12.7 mm (light green).

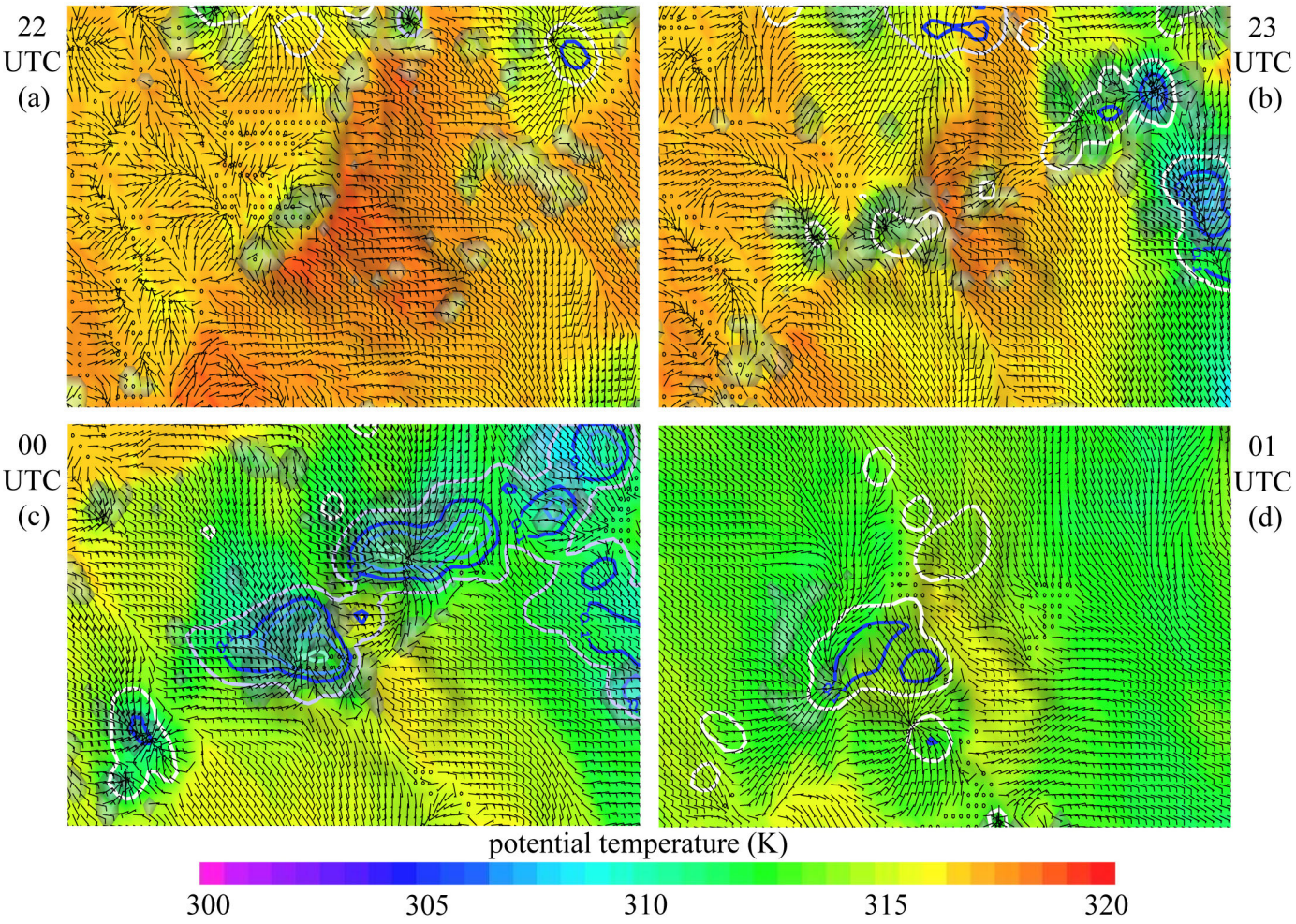

Fig. 7: As Fig. 6, but for 22-01 UTC.

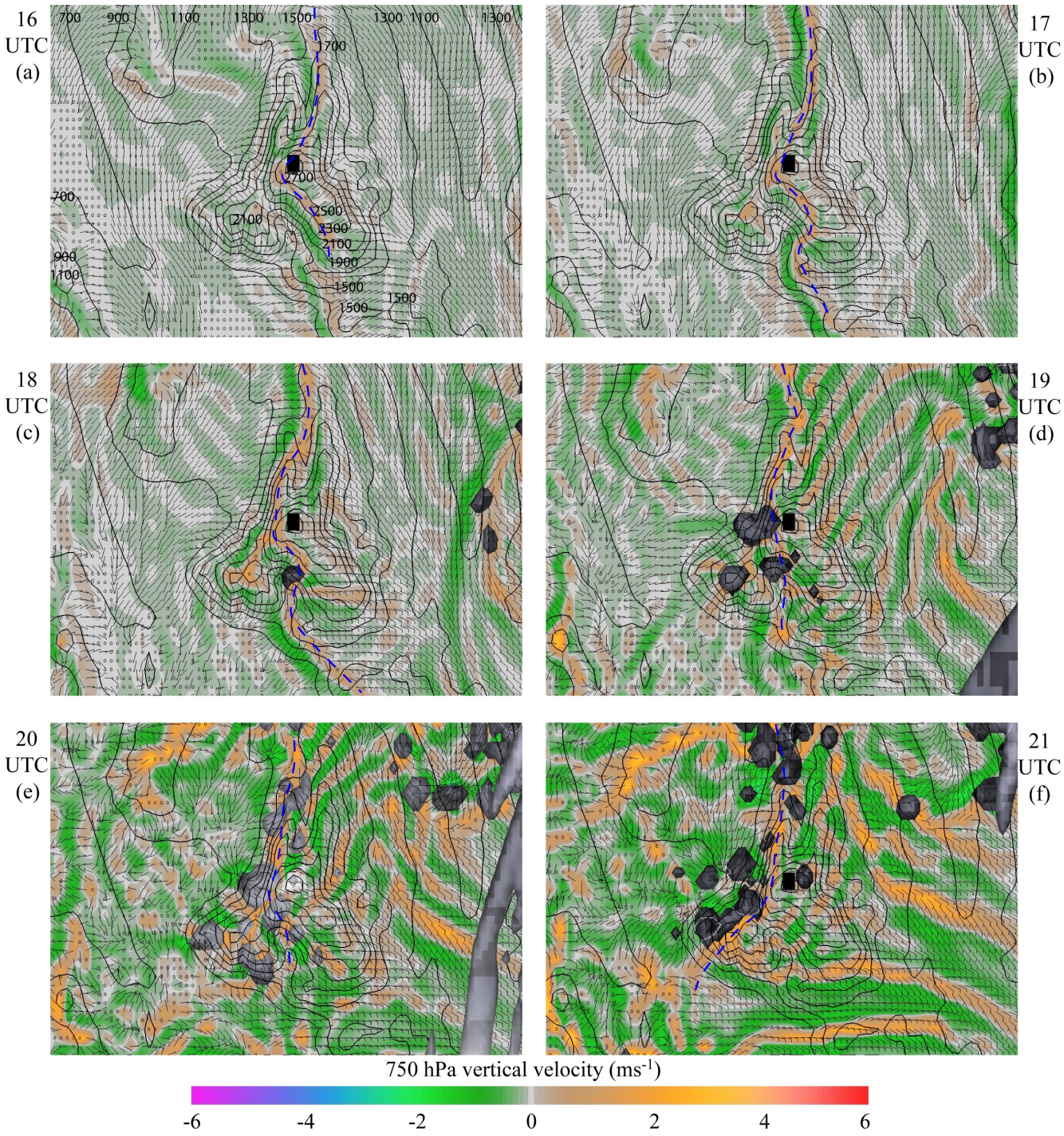

Fig. 8: Inner-domain maps of 750 hPa vertical velocity (m s^{-1}) and 10 m winds (thin barbs) for 16-21 UTC on 6 August. Also shown are the 0.01 g kg^{-1} cloud water isosurfaces, and elevation contours (black) with an interval of 200 m (labeled in (a)). The black rectangle in the vertical velocity field is due to Mt Lemmon's elevation, slightly above the 750 mb surface. The dashed blue line in each panel highlights a convergence line discussed in the text.

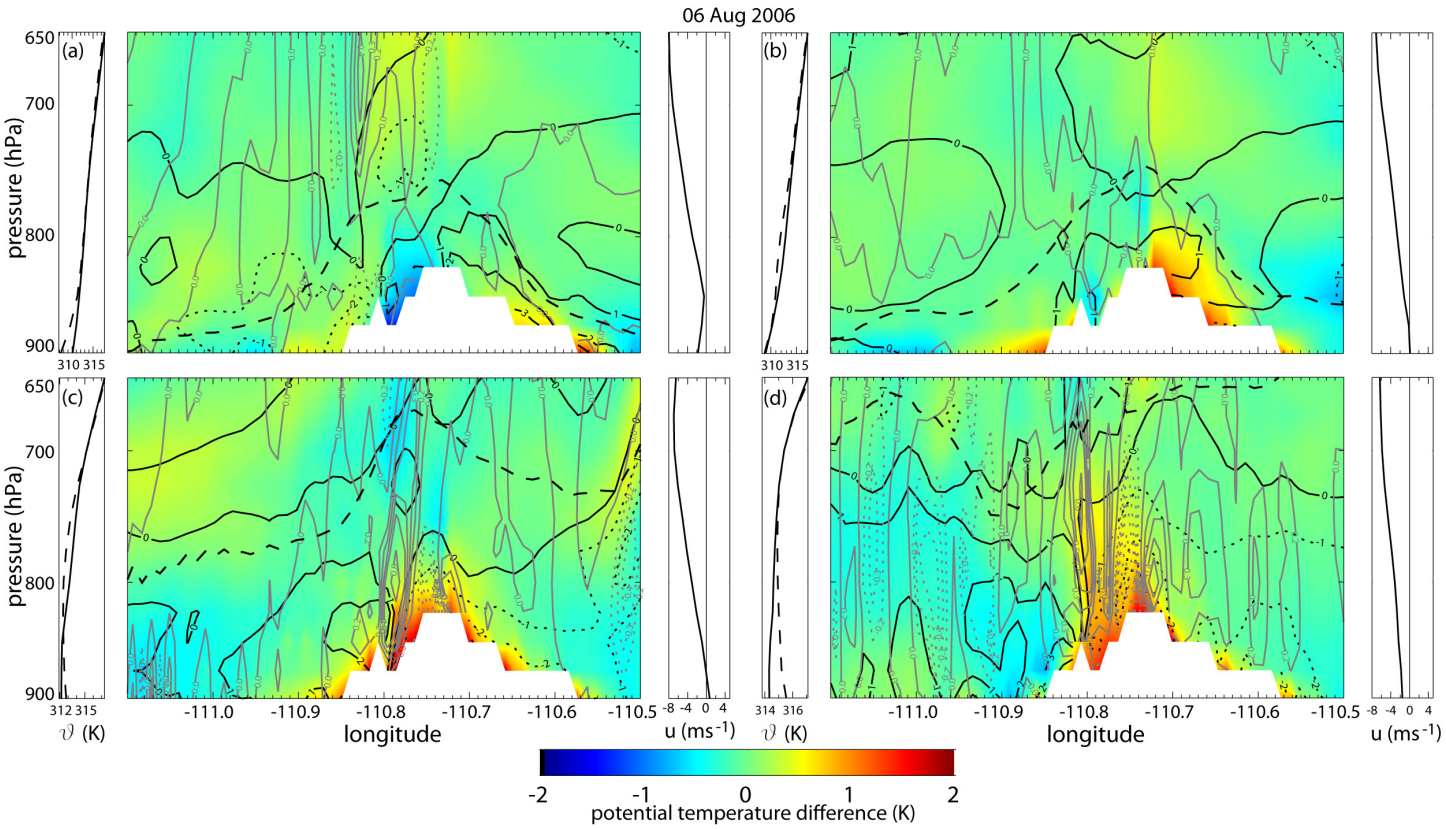

Fig. 9: East-west cross section based on averages computed over 21 km in the north-south direction for (a) 12, (b) 15, (c) 18, and (d) 21 UTC. The white area is the 21-km averaged terrain height. The cross section shows θ' (color fill), u' (solid black contours for westerly flow and dotted black contours for easterly flow, contour interval 1 m s^{-1}), w (solid grey contours for updrafts and dotted gray contours for downdrafts, contour interval 0.2 m s^{-1}) and PBL height (long-dashed black line). Also shown are profiles of $\overline{\theta_{west}}$ (solid) and $\overline{\theta_{east}}$ (dashed) on the left of each cross section, and $\overline{u}$ on the right. The variables are defined in the text.

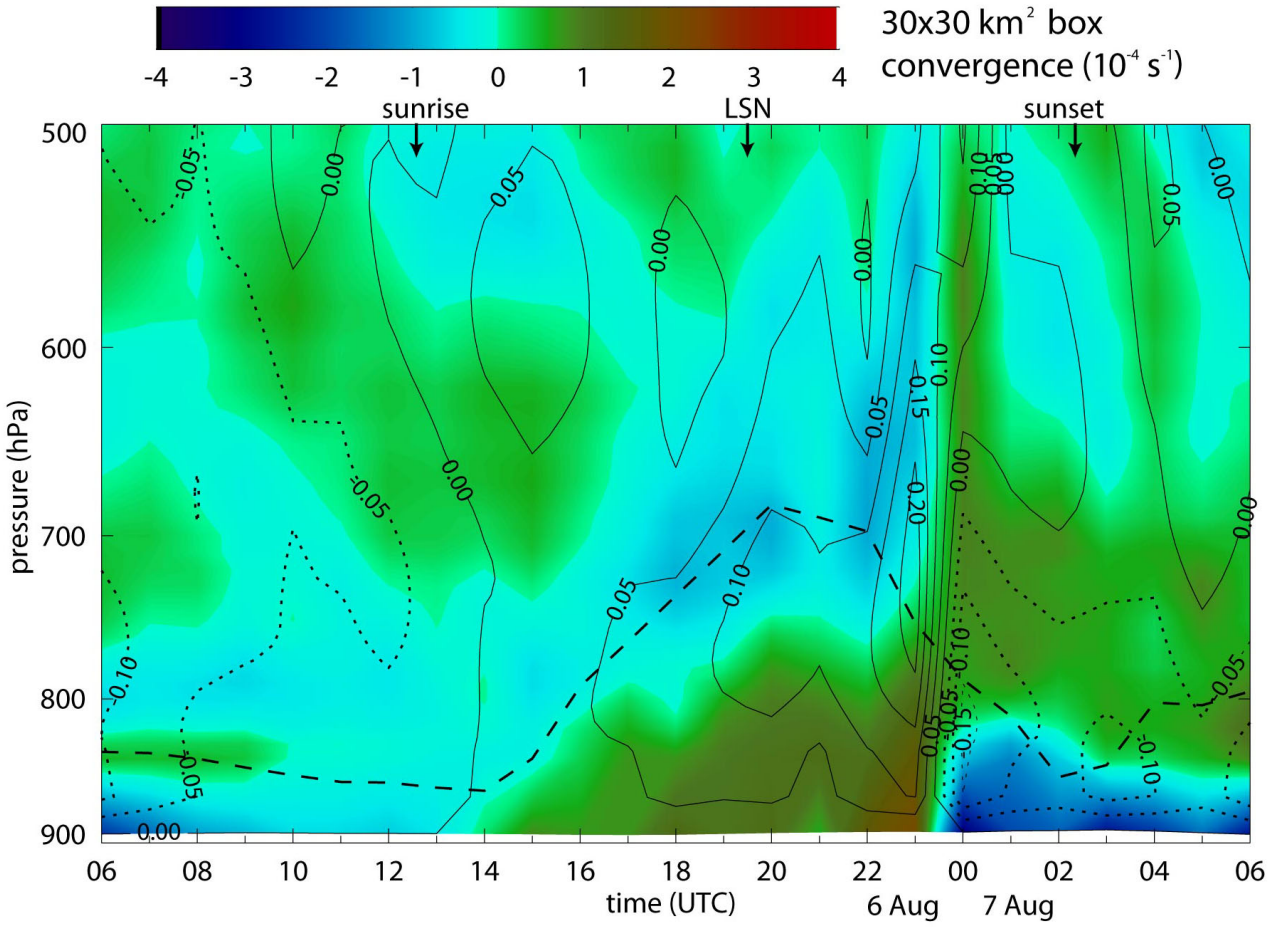

Fig. 10: Time-height plot of MSC for the 30x30 km^2 box (color shaded), mountain-scale vertical velocity within this box, inferred from mass continuity (solid lines for updrafts, dotted lines for downdrafts, contour interval 0.05 m s^{-1}), and mean PBL height within the box (bold dashed line).

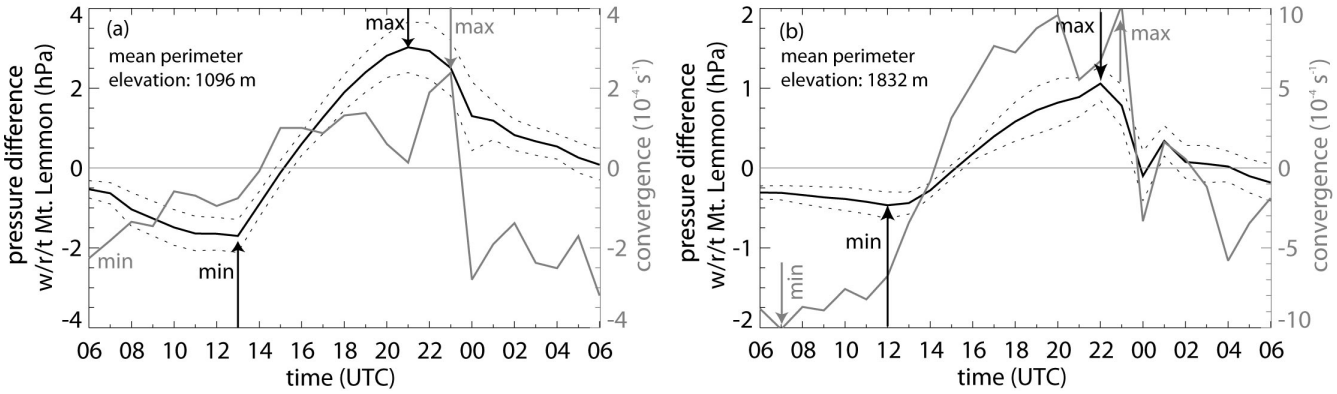

Fig. 11: (a) Time series of the mean horizontal pressure difference between points along the 30x30 km^2 box and Mt Lemmon (black solid line, left axis), and MSC for the corresponding box (grey lines, right axis), for the 6 August case. The black dotted lines indicate the mean pressure difference ± one standard deviation, based on all grid points of the box's perimeter. A positive pressure difference implies a lower pressure at Mt Lemmon, i.e. anabatic "forcing". Black arrows highlight the times of extreme pressure differences. Grey arrows highlight the same for MSC. The average height of points along the box perimeter is shown in the upper left corner. For comparison, the elevation of Mt Lemmon in the inner WRF domain is 2629 m MSL. (b) As (a), but for a 10x10 km^2 box centered on Mt Lemmon.

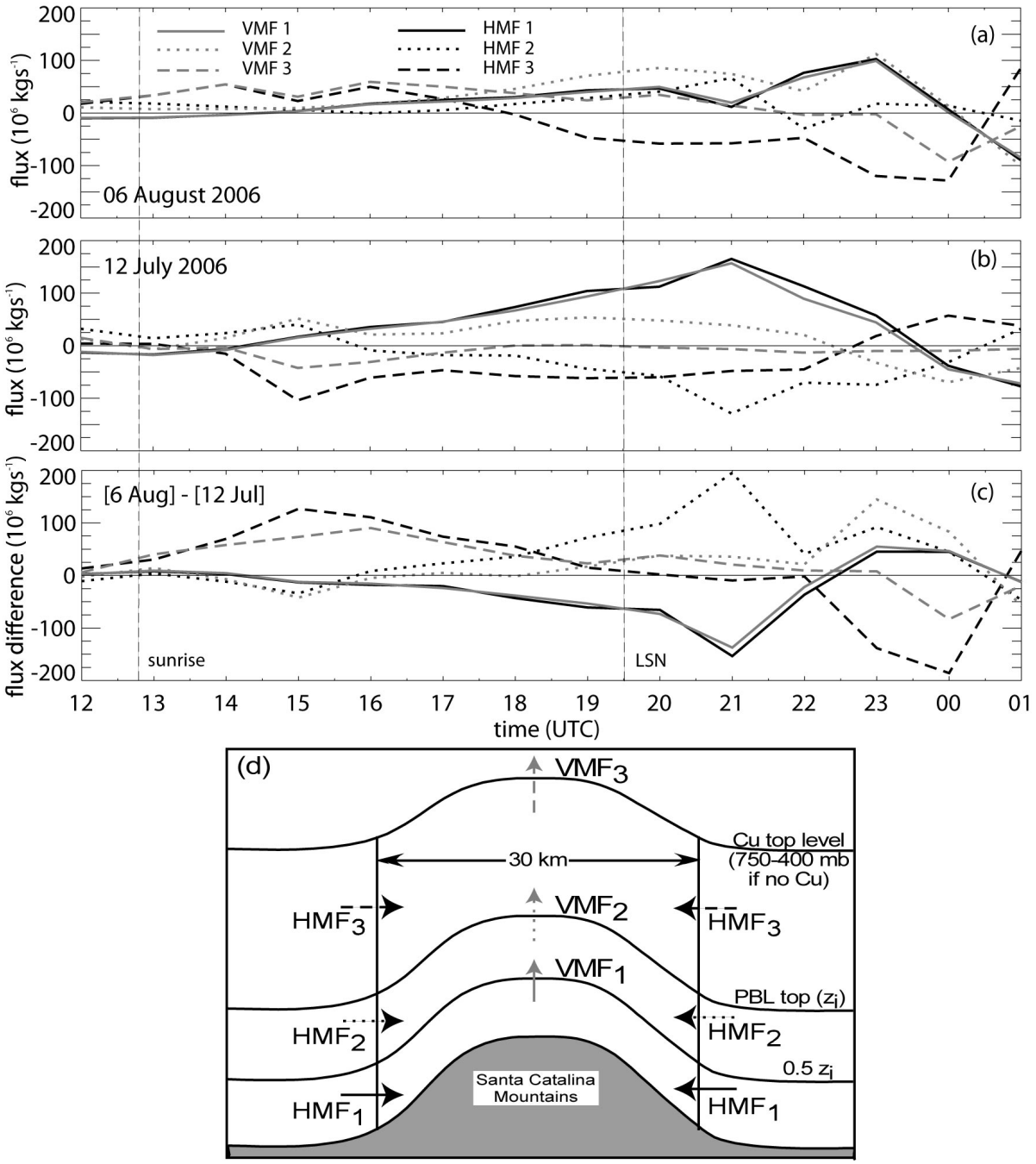

Fig. 12: Temporal variation of the horizontal and vertical mass fluxes in/out three 30x30 km^2 volumes, for (a) 6 August (a moist case), (b) 12 July (a dry case), and (c) the difference between the moist case and the dry case. The three volumes are defined in the text and illustrated in (d). Inward and upward fluxes, shown by the arrows in (d), are positive.

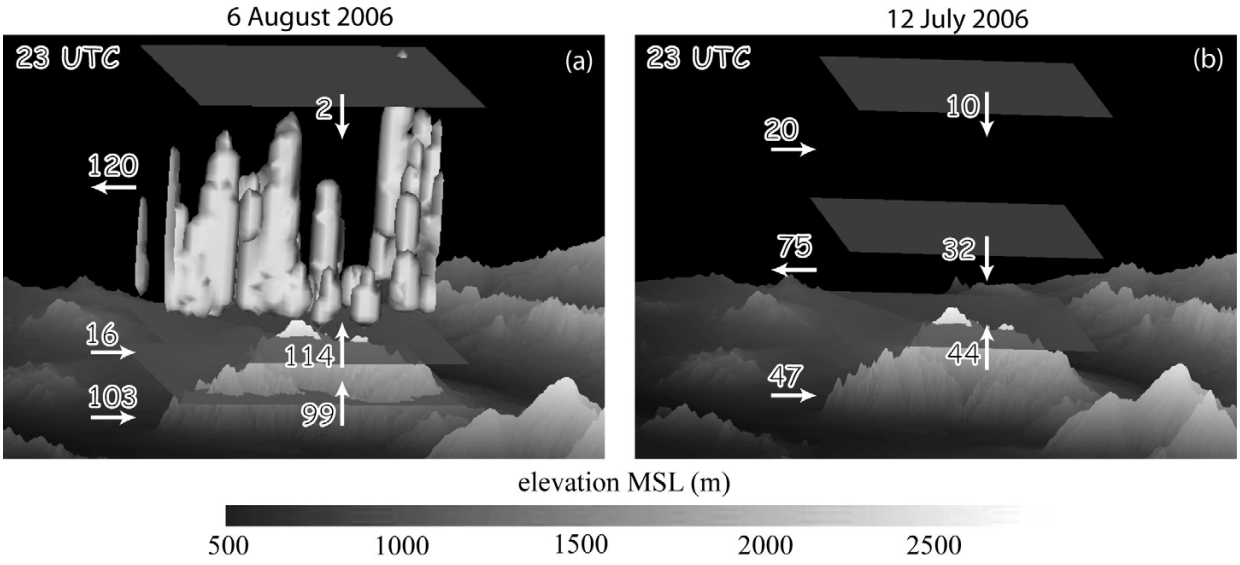

Fig. 13: Horizontal and vertical mass fluxes in/out of the three volumes shown in Fig. 12d at 23 UTC for 6 August (a) and 12 July (b). Arrows indicate the direction of flux. Flux quantities are in units of 10^6 kg s^{-1}. The terrain and 0.01 g kg^{-1} cloud isosurfaces are shown as well. The vertical boundaries of the three volumes are shown schematically as flat surfaces; in reality these boundaries are sigma surface undulating with the terrain.

Tables

Table 1: The *difference* in horizontal and vertical mass fluxes for the three volumes illustrated in Fig. 12d between the original and the no_microphysics WRF simulations, for 6 August 2006. The entire period is broken up in five periods of cumulus evolution. Since $HMF_1 \cong VMF_1$, the average of these two terms is shown as $H(V)MF_1$.

time UTC		$\boldsymbol{H(V)MF_1}$ 10^6 kg s^{-1}	$\boldsymbol{HMF_2}$ 10^6 kg s^{-1}	$\boldsymbol{HMF_3}$ 10^6 kg s^{-1}	$\boldsymbol{VMF_2}$ 10^6 kg s^{-1}	$\boldsymbol{VMF_3}$ 10^6 kg s^{-1}
12	cloud-free	0	0	-10	0	-9
13		0	-1	-9	-1	-9
14		0	-3	+9	-3	+5
15		0	-1	+1	-2	-2
16	pre-convective	+8	+5	-9	+12	+3
17		+9	-4	-10	+6	-3
18	shallow convection	+5	-7	-6	0	-6
19		-4	-1	-2	-1	-1
20		+13	-17	+14	-2	+9
21		-34	+33	+9	-2	+5
22	deep convection	+75	-59	-26	+14	-4
23		+129	+33	-154	+154	+10
00		+13	+24	-57	+37	-11
01	decay	-133	-76	+196	-194	-27

Table 2: The *difference* in horizontal and vertical heat and vapor fluxes for volumes 1 and 2 (illustrated in Fig. 12d) between 6 August and 12 July 2006, based on WRF model output. The bold numbers represent hours with moist convection over the CM on 6 August. Local solar noon at 1929 UTC.

time UTC	$\boldsymbol{HHF_1}$ tW	$\boldsymbol{HHF_2}$ tW	$\boldsymbol{HVF_2}$ 10^4 kg s^{-1}	$\boldsymbol{VHF_1}$ tW	$\boldsymbol{VHF_2}$ tW	$\boldsymbol{VVF_2}$ 10^4 kg s^{-1}
12	+1	-3	-10	+1	-1	-6
13	+3	+1	+5	+3	+4	+7
14	+1	-4	-6	+1	-2	-8
15	-4	-11	-23	-4	-13	-30
16	-6	+3	+18	-5	-2	-6
17	-7	+7	+42	-8	+1	+11
18	**-14**	**+12**	**+46**	**-13**	**-1**	**+18**
19	**-20**	**+23**	**+73**	**-18**	**+5**	**+34**
20	**-22**	**+32**	**+80**	**-25**	**+12**	**+38**
21	**-51**	**+64**	**+141**	**-46**	**+11**	**+52**
22	**-12**	**+14**	**+21**	**-8**	**+6**	**+31**
23	**+15**	**+31**	**+91**	**+16**	**+46**	**+136**
00	**+16**	**+14**	**+36**	**+15**	**+28**	**+53**
01	**-2**	**-12**	**-23**	**-4**	**-17**	**-101**

Table 3: Select water fluxes expressed as a percentage of the vertical vapor flux across the PBL top (VVF_2) during the period of precipitation at the surface.

	6 August 2006 water fluxes, expressed as a percentage of VVF_2			
	time (UTC)	$\boldsymbol{P_{sfc}}$ (precipitation efficiency)	$\boldsymbol{E_{PBL}}$	$\boldsymbol{-HVF_3}$
shallow convection	**20**	0	0	80
	21	1	25	69
deep convection	**22**	0	13	86
	23	1	17	81
	00	42	47	11
	01	10	38	52
average		**9**	**23**	**63**